The latest study by Zara et al. (2018) shows that the uncertainty of SCD is ~1.32 x 10^{15} molec/cm^2 in DOMINO v2, which is reduced to ~0.84 x 10^{15} molec/cm^2 in the newly released QA4ECV product (used for comparison here). The SCD errors are thus much smaller than the errors introduced from AMF calculation over polluted regions like China (Boersma et al., 2011; Lin et al., 2015; Lorente et al., 2017). Also, any bias in the total SCD is mostly absorbed by the stratospheric separation step, and may not propagate into the tropospheric SCD (van Geffen et al., 2015). In other words, the tropospheric SCDs used in POMINO (from DOMINO v2) are well-established. We are considering moving to using tropospheric SCDs from QA4ECV, once these have been evaluated more thoroughly (something that this paper contributes to).

We had to choose two model versions according to the availability of meteorological data – GEOS-5 data on the 0.5 x 0.667 grid were replaced by GEOS-FP on the 0.25 x 0.3125 grid after May 2013). Despite the differences in horizontal resolution and driving meteorology, the two model versions have the same vertical coordinate and use the same schemes for advection, PBL mixing and convection, which is important for vertical distribution of NO2 and aerosols. We consider the discontinuity in GEOS-Chem model resolution as a minor limitation for our NO$_2$ product for long-term trend studies.

We used the CALIOP/CALIPSO data over 2007-2015 according to data availability. Our correction of vertical profiles is on the basis of monthly climatology, thus applying the correction to other years is appropriate. Analogous approaches have been used in previous studies, for example, applying the 3-year average or 5-year average OMI surface albedo data to all years in DOMINO (Boersma et al., 2007; 2011), and applying 4-year average (2004-2007) monthly mean NO$_2$ profile shapes derived from GMI CTM simulation to retrieve tropospheric NO$_2$ in NASA's SPv2 (Bucsela et al., 2013).

MODIS AOD data were taken from two versions in our POMINO product. We agree

that using the same version of MODIS AOD data would be better. However, the difference in C5.1 and C6 is relatively small (C6 is smaller by 13.7% averaged over East China in 2012), compared to the difference between GEOS-Chem and C5.1 or between CEOS-Chem and C6. Our one-year test by using C5.1 versus C6 AOD (to correct model AOD) leads to 3.8% decrease in the retrieved NO_2 averaged over East China in 2012.

As suggested by the second reviewer, we have included the newest QA4ECV NO2 product in the revised manuscript. Figure 9, Table 2 and Table 3 have been updated accordingly. QA4ECV is biased low in cases with high aerosol loading, but its R^2 with respect to MAX-DOAS is better than DOMINO v2. This additional comparison further strengthens the importance of aerosol correction in NO_2 retrieval over East Asia. Despite its various limitations discussed here, POMINO v1.1 is closer to MAX-DOAS than QA4ECV is, especially in hazy days, highlighting the capability of POMINO v1.1.

Given these above discussions, we have decided to not release POMINO v1.1 to users. Rather, we will eventually release POMINO v2, which will include MODIS C6 merged AOD and MCD43C2 C6 daily BRDF. The POMINO v1.1 will be used as an intermediate (and the most important) step between POMINO and POMINO v2. And this paper documents how improvement in aerosol vertical distribution affects the POMINO NO_2 product, such that all other factors are consistent between POMINO and POMINO v1.1. We have clarified this point in the revised abstract and conclusion.

2. To justify the improvement in the retrieved product, authors have used a small set of MAX-DOAS measurements. Improvements are justified based on improved correlation coefficient with the POMINO product. It appears from Figure 10 that the enhanced correlation might, in fact, be driven by changes in ~6 data points only with very large (>100 x 10^15 molec cm-2) values. In many instances (for columns < 100 x 10^15 molec cm2), the agreement between OMI and MAX-DOAS appears to be better for DOMINO. Author should use different means of validation, larger set of validation datasets, and various statistical methods to assess the products.

The high values represent very polluted cases that our algorithm intends to capture. Excluding these polluted cases would lead to a substantial sampling bias over polluted regions. We have made the distinction between hazy cases and less hazy situations. The latter are more representative for retrievals over the US and Europe. In those cases, QA4ECV may perform better and POMINO is more likely to be biased high (Table 3).

We would definitely prefer to have a larger set of MAX-DOAS NO_2 data. Unfortunately, very few high-quality MAX-DOAS measurements are available over China. We have made efforts to get data from multiple sites to enhance the spatial representativeness. Our criteria to select MAX-DOAS data and OMI data mainly

follow Wang et al., (2017b) and Lin et al., (2014), who have already discussed the influence from various statistical methods.

We have included a statement in the end of Sect. 6 that "Further research may use additional MAX-DOAS datasets to evaluate the satellite products more systematically."

3. The whole discussion about processing (filtering, regridding) and comparison of CALIPSO data is distracting and unnecessary. These could be completely removed, shortened, or moved to the Appendix/Supplementary section. Also, data processing is largely subjective. Why not use more mature data assimilation technique instead?

We have revised the manuscript accordingly. The discussion on the treatment of CALIOP data has been moved to Appendix B.

Data assimilation is subject to the very limited availability of CALIOP data. It is also computationally prohibitive for our application here (multiple years over a large domain on a high-resolution grid).

Specific comments

1. Page 9, line 225: This statement may not be true. Please, replace "will not" to "may not".

Changed.

2. Page 9, line 227-231: Please be more specific on AMF calculation. What wavelength range is used for AMF for POMINO/DOMINO? I assume this is more important than the difference between online and look-up table approach.

Changed. The wavelength is 438 nm in both DOMINO and POMINO. The dependence of AMF on the wavelength is weak (actually 0.25%/nm, Boersma et al. (2018)). Other details of AMF calculations can be found in Lin et al. (2014b, 2015).

3. Page 9, line 228: This paper is all about POMINO and DOMINO. Please, say "DOMINO" instead of "in most retrieval algorithms".

As far as we know, most algorithms use look-up tables, including but not limited to NASA's SP product, DOMINO, and others participating the QA4ECV project.

4. Page 10, line 237: What are those "Other aspects"? Please, list them.

Changed.

5. Page 10, lines 237-239: This statement is likely misleading as look-up table may have been used in certain aspect of your calculation. Please, remove "without use of look-up tables".

Changed.

6. Page 10, lines 239-244, 257-259: See my general comment. The same product cannot use simulated fields from two different models. The retrievals should be based on single model.

See response to general comment.

7. Page 13, lines 314-316: How does the se of CALIPSO constraints affect cloud pressure, cloud fraction, and radiative cloud fraction? Please include relevant results and discussions.

The detailed results can be found in Sect. 4.

8. Page 13, lines 321-325: Please, clarify this statement.

Clarified.

9. Page 14, line 360: What is the justification of 2-hour averaging of MAX-DOAS? Why do you expect instantaneous OMI measurements compare well with MAX-DOAS averaged over 2-hours? Is this exercise described in the following sentences motivated to show only good results?

As already clarified in manuscript, we used the criteria based on several previous studies (Lin et al., 2014; Wang et al., 2015, 2017b). These previous papers have already discussed the most appropriate criteria to balance data coverage, passing time, spatial domain around the pixel center, etc.

10. Page 15, lines 366-367: "to some degree" is redundant.

Changed.

11. Page 15, lines 374-375: Why is this necessary? How do cloud and haze differ for their impact on measurement sensitivity of OMI?

As emphasized in the manuscript, we wanted to separate the hazy days from cloudy days. Some days are cloud-free but hazy (with heavy NO2 pollution as well). These days were filtered out in DOMINO and QA4ECV through the criteria on cloud

radiance fraction. By comparison, our algorithm was able to retain these days and avoid sampling bias (by missing polluted days) while preserving the overall accuracy of NO2 product.

As explained in the manuscript, neither the OMI cloud product nor the MODIS cloud product is able to provide the true cloud fraction, so we used the meteorological monitoring stations and the MODIS RGB product to manually check whether a day is cloudy or hazy.

12. Page 16, line 395: Please, add citations for this statement.

Changed.

13. Page 17, line 418: How does the emission strength affect the height of peak extinction?

The effect of emission strength on aerosol vertical profiles is season and location dependent. For the case here (Figure 4), emissions over Eastern China are higher in winter, in which season the atmosphere is more stagnant vertically. This means that more aerosols are concentrated near the surface, thus decreasing the height of peak extinction.

14. Page 19, lines 470-472: The spatial correlations suggest that GEOS-Chem performs very poorly in simulating aerosol fields. Why do you still use GEOS-Chem? Could not you just use CALIPSO-based aerosol information?

GEOS-Chem provides daily and spatially resolved information, which is what is needed by the satellite retrieval. CALIOP, in contrast, has poor temporal and spatial coverage, preventing fully CALIOP-based aerosol profile information to be used to retrieve the NO_2 product. The spatial correlation between GEOS-Chem and CALIOP is not as good as their temporal correlation. We thus used CALIOP for monthly climatological corrections, while retaining the GEOS-Chem simulated day-to-day variability.

Anonymous Referee #2

The paper "Improved aerosol correction for OMI tropospheric NO2 retrieval over East Asia: constraint from CALIOP aerosol vertical profile" by Liu et al. describes an improved OMI tropospheric NO2 retrieval for East China using CALIOP aerosol vertical profile information. This study updates the POMINO retrieval algorithm described in Lin et al., 2014 and 2015. Comparisons have been made between the NO2 satellite data and ground-based MAX-DOAS measurements at three sites in East-China.

The topic of the manuscript is within the scope of AMT and it is of interest to the

scientific community. It can be recommended for publication, if the authors make an effort to address the comments listed below, and improve the manuscript accordingly.

Specific comments:

Section 2.2

P9-10 The improved POMINO NO2 algorithm for China builds on the Dutch OMI NO2 v2 algorithm from 2011. The DOMINO v2 algorithm is now about 7 years old, and the authors shortly discuss some recent improvements in the satellite retrieval (e.g. improvements in the slant column retrieval). Please include the recently released "Dutch/European" OMI NO2 product provided in the framework of the QA4ECV project (v1.1) in this discussion as well (e.g. including the latest developments in the STS and the trop. AMF algorithms).

Thank you for this valuable suggestion. We have now included an evaluation of QA4ECV in the revised manuscript. Figure 9, Table 2 and Table 3 have been updated accordingly. QA4ECV is still bias low in highly polluted cases, although its R^2 with respect to MAX-DOAS is better than DOMINO v2. This additional comparison further strengthens the importance of aerosol correction in NO_2 retrieval over East Asia. POMINO v1.1 is closer to MAX-DOAS than QA4ECV is, especially in hazy days, highlighting the capability of POMINO v1.1.

P11 The authors mention that the climatological adjustments in the aerosol information is based on the assumption that systematic model limitations are month-dependent and persist over the years and days. On the other hand, the daily variations in the aerosol extinction profile are coming from the model only (Eq. 3). How good are the daily variations in the aerosol parameters modeled by GEOS-Chem?

The extent to which model aerosol information can be corrected depends on the availability of aerosol observations. MODIS and especially CALIOP suffer from low coverage on the day-to-day scale, preventing their direct use in satellite NO2 retrieval product and in daily correction of model aerosols.

Previous studies have shown that GEOS-Chem is able to simulate day-to-day variation of AOD from AERONET (Li et al., 2013, 2015) and satellite (Johnson et al., 2012), surface $PM_{2.5}$ (Liu et al., 2018), and aerosol vertical profile (Ford and Heald, 2012).

P11 From Eq. (2) and (3), I would expect a "jump" in the aerosol extinction profile from the last day of the month to the first day of the next month (because of the change in R). Is this 'jump' also noticeable in the trop. AMF and VCD?

Here we test this "jump" issue over Northern East China. For every first day in each month of year 2012, we use the monthly correction from the last month (ie. For 1st, Feb, we will use the ratio of January to adjust aerosol extinction profile of GEOS-Chem on this day). Figure R1 shows the test results. In particular, the difference in NO$_2$ VCD between this sensitivity test and our actual retrieval is below 3.8% for most cases. Besides, the distribution of VCD difference seems to be random. Thus the "jump" issue does not influence our results systematically.

We have added in the revised Sect. 2.2 that "Although this monthly adjustment means discontinuity on the day-to-day basis (e.g., from the last day of a month to the first day of the next month), such discontinuity does not affect the NO$_2$ retrieval significantly, based on our sensitivity test."
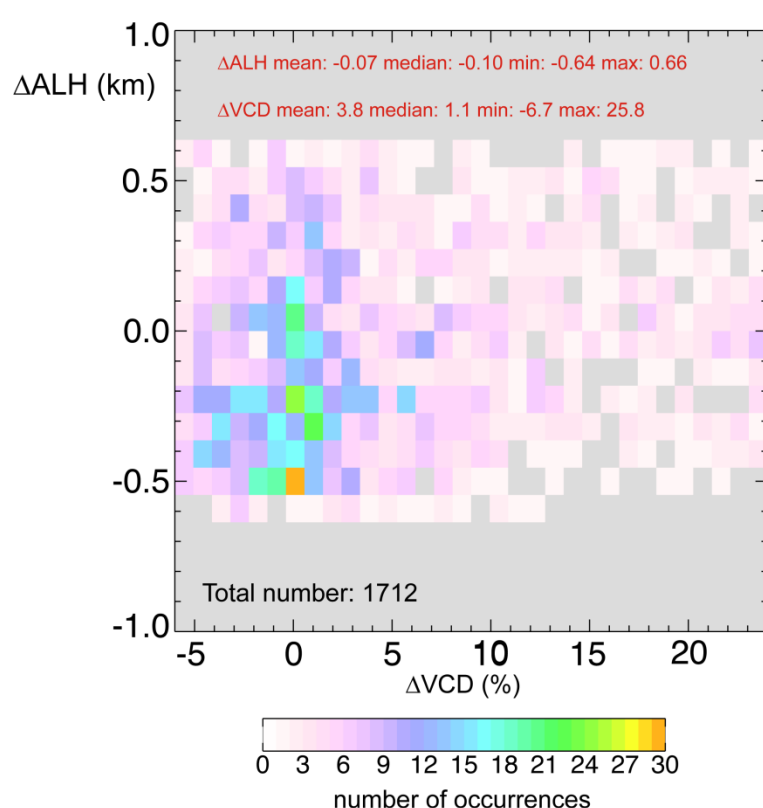
Figure R1. Percentage change in retrieved NO$_2$ VCD when using the CALIOP aerosol extinction profile in a formal month (POMINO_change) to adjust modeled profile on the first day of each month ([POMINO_change-POMINO v1.1]/[POMINO v1.1]), for each bin of ΔALH (bin size = 0.1 km) and ΔVCD (bin size = 1%) across pixels in 2012 over Northern East China. Here we only choose the pixels with WCLD < 0.5, surface albedo < 0.3 and SZA < 70⁰.

P12 How large is the effect of neglecting polarization in the RTM (LIDORT) on the trop. AMF calculation?

The impact of polarization is small, affecting stratospheric retrievals by 0.1% and reducing tropospheric AMF by < 0.5% (Boersma et al., 2011). According on Lorente et al., (2017), top-of-atmosphere reflectance simulated by four RTMs (DAK with polarization, McArtim, SCIATRAN and VLIDORT with polarization) agree within 1.5%.

Section 3.1

Fig.3 For some specific areas there seem to be large differences between the two CALIOP ALH datasets, e.g. for Shandong in summer. Is this only caused by the differences in resolution/sampling/regridding, or are there other factors?

The large difference over Shandong is persistent across the seasons. It is mainly caused by resolution/sampling/regridding process. Our climatological dataset uses the same criteria as the NASA Level-3 product does, but we aim at compiling a climatology to adjust GEOS-Chem outputs in a temporally and spatially consistent manner.

Section 4

A difficult/confusing concept of the POMINO NO2 algorithm is that for the trop. AMF, (thin) clouds are treated as reflecting boundaries in the RTM calculations (using effective cloud parameters retrieved from the O2-O2 band), while Mie parameters are used in the RTM for the layers with aerosols. It is clear that the aerosols are included in the POMINO O2-O2 cloud retrieval, but the different treatment of scattering by clouds and aerosols in the trop. AMF calculation could be addressed in more detail.

As in all other cloud products used for NO_2 retrieval, we treat clouds as "effective" Lambertian reflector with a fixed albedo (80%). Assuming Mie scattering for clouds implies an explicit treatment of vertical cloud structure, cloud droplet sizes, etc., which is actually a new direction we could explore for NO_2 retrieval.

We have added a statement in the revised Sect. 2.2: "Note that the treatment of cloud scattering (as "effective" Lambertian reflector, as in other NO_2 algorithms) is different from the treatment of aerosol scattering/absorption (vertically resolved based on the Mie scheme)."

Section 6

The evaluating of the improved OMI NO2 product with MAX-DOAS data is an important part of this study. However, the number of measurements/points in Fig. 10 seems low (e.g. compared to other satellite validation studies using the BIRA-IASB MAXDOAS data at these sites). Can the number of points be increased, e.g. by increasing the time period, relaxing the cloud screening, collocation criteria etc? Then the statistics can be improved and also time series could be added.

We would definitely prefer to have a larger set of MAX-DOAS NO_2 data. Unfortunately, very few high-quality MAX-DOAS measurements are available over China. We have made efforts to get data from multiple sites to enhance the spatial representativeness. Our criteria to select MAX-DOAS data and OMI data mainly follow Wang et al., (2017b) and Lin et al., (2014b), who have already discussed the influence from various statistical methods.

We have included a statement in the end of Sect. 6 that "Further research may use additional MAX-DOAS datasets to evaluate the satellite products more systematically."

In addition to the comparisons in Fig. 10, the MAXDOAS retrieved NO2 profiles could also be exploited with the Averaging Kernel (AK) of the OMI NO2 columns. Comparisons of the satellite NO2 columns with these "smoothed" MAXDOAS NO2 columns could provide useful additional information (e.g. to isolate the impact of the satellite a priori NO2 profile).

We only have the vertical profiles at Xianghe, with lack of spatial representativeness. Our previous study (Lin et al., 2014b) shows that using the MAX-DOAS vertical profiles have a minor impact on the retrieved NO_2.

References:

Ford, B. and Heald, C. L.: An A-train and model perspective on the vertical distribution of aerosols and CO in the Northern Hemisphere, J. Geophys. Res. Atmos., 117(D6), n/a-n/a, doi:10.1029/2011JD016977, 2012.

Johnson, M. S., Meskhidze, N. and Praju Kiliyanpilakkil, V.: A global comparison of GEOS-Chem-predicted and remotely-sensed mineral dust aerosol optical depth and extinction profiles, J. Adv. Model. Earth Syst., 4(3), M07001, doi:10.1029/2011MS000109, 2012.

Li, S., Garay, M. J., Chen, L., Rees, E. and Liu, Y.: Comparison of GEOS-Chem aerosol optical depth with AERONET and MISR data over the contiguous United States, , 118(April), 228–241, doi:10.1002/jgrd.50867, 2013.

Li, S., Chen, L., Fan, M., Tao, J., Wang, Z., Yu, C., Si, Y., Letu, H. and Liu, Y.: Estimation of GEOS-Chem and GOCART Simulated Aerosol Profiles Using CALIPSO Observations over the Contiguous United States, , (2008), 3256–3265, doi:10.4209/aaqr.2015.03.0173, 2015.

Liu, M., Lin, J., Wang, Y., Sun, Y., Zheng, B., Shao, J., Chen, L., Zheng, Y., Chen, J., Fu, M., Yan, Y., Zhang, Q. and Wu, Z.: Spatiotemporal variability of NO_2 and $PM_{2.5}$ over Eastern China: observational and model analyses with a novel statistical method, Atmos. Chem. Phys. Discuss., 2018, 1–34, doi:10.5194/acp-2017-1180, 2018.

Improved aerosol correction for OMI tropospheric NO₂ retrieval over East Asia: constraint from CALIOP aerosol vertical profile

Mengyao Liu[1,2], Jintai Lin[1], K. Folkert Boersma[2,3], Gaia Pinardi[4], Yang Wang[5], Julien Chimot[6], Thomas Wagner[5], Pinghua Xie[7,8,9], Henk Eskes[2], Michel Van Roozendael[4], François Hendrick[4], Pucai Wang[10], Ting Wang[10], Yingying Yan[1], Lulu Chen[1], Ruijing Ni[1]

1, Laboratory for Climate and Ocean-Atmosphere Studies, Department of Atmospheric and Oceanic Sciences, School of Physics, Peking University, Beijing, China

2, Royal Netherlands Meteorological Institute, De Bilt, the Netherlands

3, Meteorology and Air Quality department, Wageningen University, Wageningen, the Netherlands

4, Royal Belgian Institute for Space Aeronomy (BIRA-IASB), Brussels, Belgium

5, Max Planck Institute for Chemistry, Mainz, Germany

6, Department of Geoscience and Remote Sensing (GRS), Civil Engineering and Geosciences, TU Delft, the Netherlands

7, Anhui Institute of Optics and Fine Mechanics, Key laboratory of Environmental Optics and Technology, Chinese Academy of Sciences, Hefei, China

8, CAS Center for Excellence in Urban Atmospheric Environment, Institute of Urban Environment, Chinese Academy of Sciences, Xiamen, China

9, School of Environmental Science and Optoelectronic Technology, University of Science and Technology of China, Hefei, China

批注 [Microsof1]: Add new co-authors

23 10, IAP/CAS, Institute of Atmospheric Physics, Chinese Academy of Sciences,

24 Beijing, China

25 Correspondence to: Jintai Lin (linjt@pku.edu.cn); K. Folkert Boersma

26 (folkert.boersma@knmi.nl)

27 **Abstract**

28 Satellite retrieval of vertical column densities (VCDs) of tropospheric nitrogen dioxide

29 (NO_2) is critical for NO_x pollution and impact evaluation. For regions with high aerosol

30 loadings, the retrieval accuracy is greatly affected by whether aerosol optical effects are

31 treated implicitly (as additional "effective" clouds) or explicitly, among other factors.

32 Our previous POMINO algorithm explicitly accounts for aerosol effects to improve the

33 retrieval especially in polluted situations over China, by using aerosol information from

34 GEOS-Chem simulations with further monthly constraints by MODIS/Aqua aerosol

35 optical depth (AOD) data. Here we present a major algorithm update, POMINO v1.1,

36 by constructing a monthly climatological data set of aerosol extinction profiles, based

37 on Level-2 CALIOP/CALIPSO data over 2007–2015, to better constrain the modeled

38 aerosol vertical profiles.

39 We find that GEOS-Chem captures the month-to-month variation of CALIOP aerosol

40 layer height but with a systematic underestimate by about 300–600 m (season and

41 location dependent), due to a too strong negative vertical gradient of extinction above

42 1 km. Correcting the model aerosol extinction profiles results in small changes in

43 retrieved cloud fraction, increases in cloud top pressure (within 2–6% in most cases),

44 and increases in tropospheric NO_2 VCD by 4–16% over China on a monthly basis in

45 2012. The improved NO_2 VCDs (in POMINO v1.1) are more consistent with

46 independent ground-based MAX-DOAS observations (R^2 = 0.80, NMB = -3.4%, for

47 162 pixels in 49 days) than POMINO (R^2 = 0.80, NMB = -9.6%), DOMINO v2 (R^2 =

0.68, NMB = -2.1%) and QA4ECV (R^2 = 0.75, NMB = -22.0%) are. Especially on haze days, R^2 reaches 0.76 for POMINO v1.1, much higher than that for POMINO (0.68), DOMINO v2 (0.38) and QA4ECV (0.34). Furthermore, the increase in cloud pressure likely reveals a more realistic vertical relationship between cloud and aerosol layers, with aerosols situated above the clouds in certain months instead of always below the clouds. The POMINO v1.1 algorithm is a core step towards our next public release of data product (POMINO v2), and it will also be applied to the recently launched S5P-TropOMI sensor.

批注 [Microsof2]: Add QA4ECV results.

批注 [Microsof3]: Clarify POMINO v1.1 won't be our new released product.

1. Introduction

Air pollution is a major environmental problem in China. In particular, China has become the world's largest emitting country of nitrogen oxides (NO_X=NO+NO_2) due to its rapid economic growth, heavy industries, coal-dominated energy sources, and relatively weak emission control (Cui et al., 2016; Lin et al., 2014a; Stavrakou et al., 2016; Zhang et al., 2009). Tropospheric vertical column densities (VCDs) of nitrogen dioxide (NO_2) retrieved from the Ozone Monitoring Instrument (OMI) onboard the Earth Observing System (EOS) Aura satellite have been widely used to monitor and analyze NO_X pollution over China because of its high spatiotemporal coverage (e.g. (Lin et al., 2010; Miyazaki and Eskes, 2013; Verstraeten et al., 2015; Zhao and Wang, 2009). However, NO_2 retrieved from OMI and other space-borne instruments are subject to errors in the conversion process from radiance to VCD, particularly with respect to the calculation of tropospheric air mass factor (AMF) that is used to convert tropospheric slant column density to VCD (e.g. Boersma et al., 2011; Bucsela et al., 2013; Lin et al., 2015; Lorente et al., 2017).

Most current-generation NO_2 algorithms do not explicitly account for the effects of aerosols on NO_2 AMFs and on prerequisite cloud parameter retrievals. These retrievals often adopt an implicit approach wherein cloud algorithms retrieve "effective cloud"

3

74   parameters that include the optical effects of aerosols. This implicit method is based on

75   aerosols exerting an effect on the top-of-atmosphere radiance level, whereas the

76   assumed cloud model does not account for the presence of aerosols in the atmosphere

77   (Stammes et al., 2008; Veefkind et al., 2016; Wang et al., 2008b; Wang and Stammes,

78   2014). In the absence of clouds, an aerosol optical thickness of 1 is then interpreted as

79   an effective cloud fraction of ± 0.10, and the value also depends on the aerosol

80   properties (scattering or absorbing), true surface albedo and geometry angles (Chimot

81   et al., 2016) with an effective cloud pressure closely related to the aerosol layer, at least

82   for aerosols of predominantly scattering nature (e.g. Boersma et al., 2004, 2011,

83   Castellanos et al., 2014, 2015). However, in polluted situations with high aerosol

84   loadings and more absorbing aerosol types, which often occur over China and many

85   other developing regions, the implicit method can result in considerable biases

86   (Castellanos et al., 2014, 2015; Chimot et al., 2016; Kanaya et al., 2014; Lin et al.,

87   2014b).

88   Lin et al. (2014b, 2015) established the POMINO NO_2 algorithm, which builds on the

89   DOMINO v2 algorithm (for OMI NO_2 slant columns and stratospheric correction), but

90   improves upon it through a more sophisticated AMF calculation over China. In

91   POMINO, the effects of aerosols on cloud retrievals and NO_2 AMFs are explicitly

92   accounted for. In particular, daily information on aerosol optical properties such as

93   aerosol optical depth (AOD), single scattering albedo (SSA), phase function and

94   vertical extinction profiles are taken from nested Asian GEOS-Chem v9-02 simulations.

95   The modeled AOD at 550 nm is further constrained by MODIS/Aqua monthly AOD,

96   with the correction applied to other wavelengths based on modeled aerosol refractive

97   indices (Lin et al., 2014b). However, the POMINO algorithm does not include an

98   observation-based constraint on the vertical profile of aerosols, whose altitude relative

99   to NO_2 has strong and complex influences on NO_2 retrieval (Castellanos et al., 2015;

100   Leitão et al., 2010; Lin et al., 2014b). This study improves upon the POMINO algorithm

4

101 by incorporating CALIOP monthly climatology of aerosol vertical extinction profiles

102 to correct for model biases.

103 The CALIOP lidar, carried on the sun-synchronous CALIPSO satellite, has been

104 acquiring global aerosol extinction profiles since June 2006 (Winker et al., 2010).

105 CALIPSO and Aura are both parts of the National Aeronautics and Space

106 Administration (NASA) A-train constellation of satellites. The overpass time of

107 CALIOP/CALIPSO is only 15 minutes later than OMI/Aura. In spite of issues with the

108 detection limit, radar ratio selection and cloud contamination that cause some biases in

109 CALIOP aerosol extinction vertical profiles (Amiridis et al., 2015; Koffi et al., 2012;

110 Winker et al., 2013), comparisons of aerosol extinction profiles between ground-based

111 lidar and CALIOP show good agreements (Kacenelenbogen et al., 2014; Kim et al.,

112 2009; Misra et al., 2012). However, CALIOP is a nadir-viewing instrument that

113 measures the atmosphere along the satellite ground-track with a narrow field-of-view.

114 This means that the daily geographical coverage of CALIOP is much smaller than that

115 of OMI. Thus previous studies often used monthly/seasonal regional mean CALIOP

116 data to study aerosol vertical distributions or to evaluate model simulations (Chazette

117 et al., 2010; Johnson et al., 2012; Koffi et al., 2012; Ma and Yu, 2014; Sareen et al.,

118 2010).

119 There exist a few CALIOP Level-3 gridded datasets, such as LIVAS (Amiridis et al.

120 2015) and NASA official Level-3 monthly dataset (Winker et al., 2013). However,

121 LIVAS is an annual average day-night combined product, not suitable to be applied to

122 OMI NO_2 retrievals (around early afternoon, and in need of a higher temporal resolution

123 than annual). The horizontal resolution (2° long. × 5° lat.) of NASA official product

124 is much coarser than OMI footprints and the GEOS-Chem model resolution.

批注 [Microsof4]: Clarify our statements

125 Here we construct a custom monthly climatology of aerosol vertical extinction profiles

126 based on 9-years (2007–2015) worth of CALIOP Version 3 Level-2 532 nm data. On a

127   climatological basis, we use the CALIOP monthly data to adjust GEOS-Chem profiles

128   in each grid cell for each day of the same month in any year. We then use the corrected

129   GEOS-Chem vertical extinction profiles in the retrievals of cloud parameters and NO_2.

130   Finally, we evaluate our updated POMINO retrieval (hereafter referred to as POMINO

131   v1.1), our previous POMINO product, DOMINO v2 and the newly released Quality

132   ==Assurance for Essential Climate Variables product (QA4ECV, see Appendix A)==, using

133   ground-based MAX-DOAS NO_2 column measurements at three urban/suburban sites

134   in East China for the year of 2012 and several months in 2008/2009.

135   Section 2 describes the construction of CALIOP aerosol extinction vertical profile

136   monthly climatology, the POMINO v1.1 retrieval approach, and the MAX-DOAS data.

137   It also presents the criteria for comparing different NO_2 retrieval products and for

138   selecting coincident OMI and MAX-DOAS data. Section 3 compares our CALIOP

139   climatology with NASA's official Level-3 CALIOP dataset and GEOS-Chem

140   simulation results. Sections 4 and 5 compare POMINO v1.1 to POMINO to analyze the

141   influence of improved aerosol vertical profiles on retrievals of cloud parameters and

142   NO_2 VCDs, respectively. Section 6 evaluates POMINO, POMINO v1.1, DOMNO v2

143   and QA4ECV NO_2 VCD products using the MAX-DOAS data. Section 7 concludes

144   our study.

145   **2. Data and methods**

146   2.1 CALIOP monthly mean extinction profile climatology

147   CALIOP is a dual-wavelength polarization lidar measuring attenuated backscatter

148   radiation at 532 and 1064 nm since June 2006. The vertical resolution of aerosol

149   extinction profiles is 30 m below 8.2 km and 60 m up to 20.2 km (Winker et al., 2013),

150   with a total of 399 sampled altitudes. The horizontal resolution of CALIOP scenes is

151 335 m along the orbital track and is given over a 5 km horizontal resolution in Level-2
152 data.

153 As detailed in Appendix B, we use the daily all-sky Version 3 CALIOP Level-2 aerosol
154 profile product at 532 nm from 2007 to 2015 to construct a monthly Level-3
155 climatological dataset of aerosol extinction profiles over China and nearby regions.
156 This dataset is constructed on the GEOS-Chem model grid (0.667° long. x 0.5° lat.)
157 and vertical resolution (47 layers, with 36 layers or so in the troposphere). The ratio of
158 climatological monthly CALIOP to monthly GEOS-Chem profiles represents the
159 scaling profile to adjust the daily GEOS-Chem profiles in the same month (see Sect.
160 2.2)

161 *2.2 POMINO v1.1 retrieval approach*

162 The NO_2 retrieval consists of three steps. First, the total NO_2 slant columns density
163 (SCD) is retrieved using the Differential Optical Absorption Spectroscopy (DOAS)
164 technique (for the 405-465 nm spectral window in the case of OMI). The uncertainty
165 of the SCD is determined by the appropriateness of the fitting technique, the instrument
166 noise, the choice of fitting window, and the orthogonality of the absorbers' cross
167 sections (Bucsela et al., 2006; van Geffen et al., 2015; Lerot et al., 2010; Richter et al.,
168 2011; Zara et al., 2018). The NO_2 SCD in DOMINO v2 has a bias at about $0.5\sim1.3 \times$
169 10^{15} molec. cm^{-2} (Belmonte Rivas et al., 2014; Dirksen et al., 2011; van Geffen et al.,
170 2015; Marchenko et al., 2015; Zara et al., 2018), which can be reduced by improving
171 wavelength calibration and including O_2-O_2 and liquid water absorption in the fitting
172 model (van Geffen et al., 2015; Zara et al., 2018). The tropospheric SCD is then
173 obtained by subtracting the stratospheric SCD from the total SCD. The bias in the total
174 SCD is mostly absorbed by this stratospheric separation step, which may not propagate
175 into the tropospheric SCD (van Geffen et al., 2015). The last step converts the
176 tropospheric SCD to VCD by using the tropospheric AMF (VCD = SCD / AMF). The

177   tropospheric AMF is calculated at 438 nm by using look-up tables (in most retrieval

178   algorithms) or online radiative transfer modeling (in POMINO) driven by ancillary

179   parameters, which act as the dominant source of errors in retrieved NO_2 VCD data over

180   polluted areas (Boersma et al., 2007; Lin et al., 2014b, 2015; Lorente et al., 2017).

181   Our POMINO algorithm focuses on the tropospheric AMF calculation over China and

182   nearby regions, taking the tropospheric SCD (Dirksen et al., 2011) from DOMINO v2

183   (Boersma et al., 2011). POMINO improves upon the DOMINO v2 algorithm in the

184   treatment of aerosols, surface reflectance, online radiative transfer calculations, spatial

185   resolution of NO_2, temperature and pressure vertical profiles, and consistency between

186   cloud and NO_2 retrievals (Lin et al., 2014b, 2015). In brief, we use the parallelized

187   LIDORT-driven AMFv6 package to derive both cloud parameters and tropospheric

188   NO_2 AMFs for individual OMI pixels online. NO_2 vertical profiles, aerosol optical

189   properties and aerosol vertical profiles are taken from the nested GEOS-Chem model

190   over Asia (0.667 ° long.×0.5° lat. before May 2013 and 0.3125 ° long.×0.25 ° lat.

191   afterwards), and pressure and temperature profiles are taken from the GEOS-5 and

192   GEOS-FP assimilated meteorological fields that drive GEOS-Chem simulations.

193   Model aerosols are further adjusted by satellite data (see below). We adjust the pressure

194   profiles based on the difference in elevation between the pixel center and the matching

195   model grid cell (Zhou et al., 2010). We also account for the effects of surface

196   bidirectional reflectance distribution function (BRDF) (Lin et al., 2014b; Zhou et al.,

197   2010) by taking three kernel parameters (isotropic, volumetric and geometric) from the

198   MODIS MCD43C2 data set at 440 nm (Lucht et al., 2000).

199   As a prerequisite to the POMINO NO_2 retrieval, clouds are retrieved through the O_2-

200   O_2 algorithm (Acarreta et al., 2004; Stammes et al., 2008) with O_2-O_2 SCDs from

201   OMCLDO2, and with pressure, temperature, surface reflectance, aerosols and other

202   ancillary information consistent with the NO_2 retrieval. Note that the treatment of cloud

203 scattering (as "effective" Lambertian reflector, as in other NO_2 algorithms) is different

204 from the treatment of aerosol scattering/absorption (vertically resolved based on the

205 Mie scheme).

206 POMINO uses the temporally and spatially varying aerosol information, including

207 AOD, single scattering albedo (SSA), phase function and vertical profiles from GEOS-

208 Chem simulations. POMINO v1.1 (this work) further uses CALIOP data to constrain

209 the shape of aerosol vertical extinction profile. We run the model at a resolution of

210 0.3125° long.×0.25° lat. before May 2013 and 0.667° long.×0.5° lat. afterwards, as

211 determined by the resolution of the driving meteorological fields. We then regrid the

212 finer resolution model results to 0.667° long.×0.5° lat., to be consistent with the

213 CALIOP data grid. We then sample the model data at times and locations with valid

214 CALIOP data at 532 nm to establish the model monthly climatology.

215 For any month in a grid cell, we divide the CALIOP monthly climatology of aerosol

216 extinction profile shape by model climatological profile shape to obtain a unitless

217 scaling profile (Eq. 1), and apply this scaling profile to all days of that month in all

218 years (Eq. 2). Such a climatological adjustment is based on the assumption that

219 systematic model limitations are month-dependent and persist over the years and days

220 (e.g., a too strong vertical gradient, see Sect. 3.3). Although this monthly adjustment

221 means discontinuity on the day-to-day basis (e.g., from the last day of a month to the

222 first day of the next month), such discontinuity does not significantly affect the NO_2

223 retrieval, based on our sensitivity test.

224 In Eqs. 1 and 2, E^C represents the CALIOP climatological aerosol extinction

225 coefficient, E^G the GEOS-Chem extinction, E^{Gr} the post-scaling model extinction,

226 and R the scaling profile. The subscript i denotes a grid cell, k a vertical layer, d a day,

227 m a month, and y a year. Note that in Eq. 1, the extinction coefficient at each layer is

228 normalized relative to the maximum value of that profile. This procedure ensures that

9

229   the scaling is based on the relative shape of the extinction profile and is thus

230   independent of the accuracies of CALIOP and GEOS-Chem AOD. We keep the

231   absolute AOD value of GEOS-Chem unchanged in this step.

232   $R_{i,k,m} = \dfrac{E^C_{i,k,m}/\max(E^C_{i,k,m})}{E^G_{i,k,m}/max(E^G_{i,k,m})}$ (1)

233   $E^{Gr}_{i,k,d,m,y} = E^G_{i,k,d,m,y} \times R_{i,k,m}$ (2)

234   In POMINO, the GEOS-Chem AOD are further constrained by a MODIS/Aqua

235   Collection 5.1 monthly AOD dataset compiled on the model grid (Lin et al., 2014b,

236   2015). POMINO v1.1 uses the Collection 5.1 AOD data before May 2013 and

237   Collection 6 data afterwards. For adjustment, model AOD are projected to a

238   $0.667°$ long.$\times 0.5°$ lat. grid and then sampled at times and locations with valid MODIS

239   data (Lin et al., 2015). As shown in Eq. 3, τ^M denotes MODIS AOD, τ^G GEOS-

240   Chem AOD, and τ^{Mr} post-adjustment model AOD. The subscript i denotes a grid

241   cell, d a day, m a month, and y a year. This AOD adjustment ensures that in any month,

242   monthly mean GEOS-Chem AOD is the same as MODIS AOD while the modeled day-

243   to-day variability is kept.

244   $\tau^{Gr}_{i,d,m,y} = \dfrac{\tau^M_{i,m,y}}{\tau^G_{i,m,y}} \times \tau^G_{i,d,m,y}$ (3)

245   Equations 4–5 show the complex effects of aerosols in calculating the AMF for any

246   pixel. The AMF is the linear sum of tropospheric layer contributions to the slant column

247   weighted by the vertical sub columns (Eq. 4). The box AMF, amf_k, describes the

248   sensitivity of NO$_2$ SCD to layer k, and $x_{a,k}$ represent the subcolumn of layer k from

249   a priori NO$_2$ profile. The l represent the first integrated layer, which is the layer above

250   the ground for clear sky, or the layer above cloud top for cloudy sky. The t represent

251   the tropopause layer. POMINO assumes the independent pixel approximation (IPA)

10

252　(Martin et al., 2002; Boersma et al., 2002). This means that the calculated AMF for any

253　pixel consists of a fully cloudy-sky portion (AMF_{clr}) and a fully clear-sky portion

254　(AMF_{cld}), with weights based on the cloud radiance fraction (CRF = $(1 - CF) \cdot A_{clr}$ +

255　$CF \cdot A_{cld}$, where A_{clr}, A_{cld} are radiance from the clear-sky part and fully cloudy part

256　of the pixel, respectively.) (Eq. 5). AMF_{cld} is affected by above-cloud aerosols, and

257　AMF_{clr} is affected by aerosols in the entire column. Also, aerosols affect the retrieval

258　of CRF. Thus, the improvement of aerosol vertical profile in POMINO v1.1 affects all

259　the three quantities in Eq. 5 and thus leads to complex impacts on retrieved NO_2 VCD.

260　$AMF = \frac{\sum_l^t amf_k x_{a,k}}{\sum_l^t x_{a,k}}$　(4)

261　$AMF = AMF_{cld} \cdot CRF + AMF_{clr} \cdot (1 - CRF)$　(5)

262　2.3 OMI pixel selection to evaluate POMINO v1.1, POMINO, DOMINO v2 and

263　QA4ECV

264　We exclude OMI pixels affected by row anomaly (Schenkeveld et al., 2017) or with

265　high albedo caused by icy/snowy ground. To screen out cloudy scenes, we choose

266　pixels with CRF below 50% (effective cloud fraction is typically below 20%) in

267　POMINO.

268　The selection of CRF threshold influences the validity of pixels. The "effective" CRF

269　in DOMINO implicitly includes the influence of aerosols. In POMINO, the aerosol

270　contribution is separated from that of the clouds, resulting in a lower CRF than for

271　DOMINO. The CRF differs insignificantly between POMINO and POMINO v1.1,

272　because the same AOD and other non-aerosol ancillary parameters are used in the

273　retrieval process. Using the CRF from POMINO instead of DOMINO or QA4ECV for

274　cloud screening means that the number of "valid" pixels in DOMINO increases by

275　about 25%, particularly because much more pixels with high pollutant (aerosol and NO_2)

11

批注 [Microsof6]: Add explanation for CRF.

276 loadings are now included. This potentially reduces the sampling bias (Lin et al., 2014b,

277 2015), and the ensemble of pixels now includes scenes with high "aerosol radiative

278 fractions". Further research is needed to fully understand how much these high-aerosol

279 scenes may be subject to the same screening issues as the cloudy scenes. Nevertheless,

280 the limited evidence here and in Lin et al. (2014b, 2015) suggests that including these

281 high-aerosol scenes does not affect the accuracy of NO_2 retrieval.

282 2.4 MAX-DOAS data

283 We use MAX-DOAS measurements at three suburban or urban sites in East China,

284 including one urban site at the Institute of Atmospheric Physics (IAP) in Beijing

285 (116.38° E, 39.38 ° N), one suburban site in Xianghe County (116.96° E, 39.75 ° N)

286 to the south of Beijing, and one urban site in the Wuxi City (120.31° E, 31.57 ° N) in

287 the Yangzi River delta (YRD). Figure 1 shows the locations of these sites overlaid with

288 POMINO v1.1 NO_2 VCDs in August 2012. Table 1 summarizes the information of

289 MAX-DOAS measurements.

290 The instruments in IAP and in Xianghe were designed at BIRA-IASB (Clémer et al.,

291 2010). Such an instrument is a dual-channel system composed of two thermally

292 regulated grating spectrometers, covering the ultraviolet (300–390 nm) and visible

293 (400–720 nm) wavelengths. It measures scattered sunlight every 15 minutes at nine

294 elevation angles: 2°, 4°, 6°, 8°, 10°, 12°, 15°, 30°, and 90°. The telescope

295 of the instrument is pointed to the north. The data are analyzed following Hendrick et

296 al. (2014). The Xianghe suburban site is influenced by pollution from the surrounding

297 major cities like Beijing and Tianjin. At Xianghe, MAX-DOAS data are data are

298 continuously available since early 2011, and data in 2012 are used here for comparison

299 with OMI products. At IAP, MAX-DOAS data are available in 2008 and 2009 (Table

300 1), thus for comparison purposes we process OMI products to match the MAX-DOAS

301 times.

302   Located on the roof of an 11-story building, the instrument at Wuxi was developed by

303   Anhui Institute of Optics and Fine Mechanics (AIOFM) (Wang et al., 2015, 2017a). Its

304   telescope is pointed to the north and records at five elevation angles (5°, 10°, 20°,

305   30° and 90°). Wuxi is a typical urban site affected by heavy NO_x and aerosol

306   pollution. The measurements used here are analyzed in Wang et al. (2017a). Data are

307   available in 2012 for comparison with OMI products.

308   When comparing the four OMI products against MAX-DOAS observations, temporal

309   and spatial inconsistency in sampling is inevitable. The spatial inconsistency, together

310   with the substantial horizontal inhomogeneity in NO_2, might be more important than

311   the influence of temporal inconsistency (Wang et al., 2017b). The influence of the

312   horizontal inhomogeneity was suggested to be about 10–30% for MAX-DOAS

313   measurements in Beijing (Lin et al., 2014b; Ma et al., 2013) and 10–15% for less

314   polluted locations like Tai'an, Mangshan and Rudong (Irie et al., 2012). Following

315   previous studies (Lin et al., 2014b; Wang et al., 2015, 2017b), we average MAX-DOAS

316   data within 2 h of the OMI overpass time, and we select OMI pixels within 25 km of a

317   MAX-DOAS site whose viewing zenith angle is below 30°. To exclude local pollution

318   events near the MAX-DOAS site (such as the abrupt increase of NO_2 caused by the

319   pass of consequent vehicles during a very short period), the standard deviation of MAX-

320   DOAS data within 2 h should not exceed 20% of their mean value (Lin et al., 2014b).

321   We elect not to spatially average the OMI pixels because they can, to some degree,

322   reflect the spatial variability in NO_2 and aerosols.

323   We further exclude MAX-DOAS data in cloudy conditions, as clouds can cause large

324   uncertainties in MAX-DOAS and OMI data. To find the actual cloudy days, we use

325   MODIS/Aqua cloud fraction data, MODIS/Aqua Level-3 corrected reflectance (true

326   color) data at the $1° \times 1°$ resolution, and current weather data observed from the

327   nearest ground meteorological station (indicated by the black triangles in Fig. 1b).

13

328   Since there is only one meteorological station available near the Beijing area, it is used

329   for both IAP and Xianghe MAX-DOAS sites. We first use MODIS/Aqua corrected

330   reflectance (true color) to distinguish clouds from haze. For cloudy days determined by

331   the reflectance checking, we examine both the MODIS/Aqua cloud fraction data and

332   the meteorological station cloud records, considering that MODIS/Aqua cloud fraction

333   data may be missing or have a too coarse horizontal resolution to accurately interpret

334   the cloud conditions at the MAX-DOAS site. We exclude MAX-DOAS NO_2 data if the

335   MODIS/Aqua cloud fraction is larger than 60% and the meteorological station reports

336   a "BROKEN" (cloud fraction ranges from 5/8 to 7/8) or "OVERCAST" (full cloud

337   cover) sky. For the three MAX-DOAS sites together, this leads to 49 days with valid

338   data out of 64 days with pre-screening data.

339   We note here that using cloud fraction data from MODIS/Aqua or MAX-DOAS (for

340   Xianghe only, see Gielen et al., 2014) alone to screen cloudy scenes may not be

341   appropriate on heavy-haze days.   For example, on 8th January, 2012, MODIS/Aqua

342   cloud fraction is about 70–80% over the North China Plain and MAX-DOAS at

343   Xianghe suggests the presence of "thick clouds". However, both the meteorological

344   station and MODIS/Aqua corrected reflectance (true color) product suggest that the

345   North China Plain was covered by a thick layer of haze. Consequently, this day was

346   excluded from the analysis.

347   **3. Monthly climatology of aerosol extinction profiles from CALIOP and GEOS-**

348   **Chem**

349   3.1 CALIOP monthly climatology

350   The aerosol layer height (ALH) is a good indicator to what extent aerosols are mixed

351   vertically (Castellanos et al., 2015). As defined in Eq. A1 in Appendix B, the ALH is

352   the average height of aerosols weighted by vertically resolved aerosol extinction. Figure

14

353 2a shows the spatial distribution of our CALIOP ALH climatology in each season. At

354 most places, the ALH reaches a maximum in spring or summer and a minimum in fall

355 or winter. The lowest ALH in fall and winter can be attributed to heavy near-surface

356 pollution and weak vertical transport. The high values in summer are related to strong

357 convective activities. Over the north, the high values in spring are partly associated with

358 Asian dust events, due to high surface winds and dry soil in this season (Huang et al.,

359 2010; Proestakis et al., 2017; Wang et al., 2010), which also affects the oceanic regions

360 via atmospheric transport. The springtime high ALH over the south may be related to

361 the transport of carbonaceous aerosols from Southeast Asian biomass burning (Jethva

362 et al., 2016). Averaged over the domain, the seasonal mean ALHs are 1.48 km, 1.43

363 km, 1.27km, 1.18 km in spring, summer, fall and winter.

364 Figure 3a,b further shows the climatological monthly variations of ALH averaged over

365 Northern East China (the anthropogenic source region shown in orange in Fig. 1a) and

366 Northwest China (the dust source region shown in yellow in Fig. 1a). The two regions

367 exhibit distinctive temporal variations. Over Northern East China, the ALH reaches a

368 maximum in April (~1.53 km) and a minimum in December (~1.14 km). Over

369 Northwest China, the ALH peaks in August (~1.59km) because of strongest convection

370 (Zhu et al., 2013), although the springtime ALH is also high.

371 Figure 4a shows the climatological seasonal regional average vertical profiles of aerosol

372 extinction over Northern East China. Here, the aerosol extinction increases from the

373 ground level to a peak at about 300–600 m (season dependent), above which it

374 decreases gradually. The height of peak extinction is lowest in winter, consistent with

375 a stagnant atmosphere, thin mixing layer, and increased emissions (from residential and

376 industrial sectors). The large error bars (horizontal lines in different layers, standing for

377 1 standard deviation) indicate strong spatiotemporal variability of aerosol extinction.

378 Over Northwest China (Fig. 5a), the column total aerosol extinction is much smaller
379 than that over Northern East China (Fig. 4a), due to lower anthropogenic sources and
380 dominant natural dust emissions. Vertically, the decline of extinction from the peak-
381 extinction height to 2 km is also much more gradual than the decline over Northern East
382 China, indicating stronger lifting of surface emitted aerosols. In winter, the column total
383 aerosol extinction is close to the high value in dusty spring, whereas the vertical
384 gradient of extinction is strongest among the seasons. This reflects the high
385 anthropogenic emissions in parts of Northwest China, which have been rapidly
386 increasing in the 2000s due to relatively weak emission control supplemented by
387 growing activities of relocation of polluted industries from the eastern coastal regions
388 (Cui et al., 2016; Zhao et al., 2015).

389 Overall, the spatial and seasonal variations of CALIOP aerosol vertical profiles are
390 consistent with changes in meteorological conditions, anthropogenic sources, and
391 natural emissions. The data will be used to evaluate and adjust GEOS-Chem simulation
392 results in Sect. 3.2. A comparison of our CALIOP dataset with NASA's official Level-
393 3 data is presented in Appendix C.

394 3.2 Evaluation of GEOS-Chem aerosol extinction profiles

395 Figure 2b shows the spatial distribution of seasonal ALHs simulated by GEOS-Chem.
396 The model captures the spatial and seasonal variations of CALIOP ALH (Fig. 2a) to
397 some degree, with an underestimate by about 0.3 km on average.   The spatial
398 correlation between CALIOP (Fig. 2a) and GEOS-Chem (Fig. 2b) ALH is 0.37 in
399 spring, 0.57 in summer, 0.40 in fall, and 0.44 in winter. The spatiotemporal consistency
400 and underestimate is also clear from the regional mean monthly ALH data in Fig. 3 –
401 the temporal correlation between GEOS-Chem and CALIOP ALH is 0.90 in Northern
402 East China and 0.97 in Northwest China.

403   Figures 4a and 5a show the GEOS-Chem simulated 2007–2015 monthly climatological

404   vertical profiles of aerosol extinction coefficient over Northern East China and

405   Northwest China, respectively. Over Northern East China (Fig. 4a), the model (red line)

406   captures the vertical distribution of CALIOP extinction (black line) below the height of

407   1 km, despite a slight underestimate in the magnitude of extinction and an overestimate

408   in the peak-extinction height. From 1 to 5 km above the ground, the model substantially

409   overestimates the rate of decline in extinction coefficient with increasing altitude.

410   Across the seasons, GEOS-Chem underestimates the magnitude of aerosol extinction

411   by up to 37% (depending on the height). Over Northwest China (Fig. 5a), GEOS-Chem

412   has an underestimate in all seasons, with the largest bias by about 80% in winter likely

413   due to underestimated water-soluble aerosols and dust emissions (Li et al., 2016; Wang

414   et al., 2008a).

415   Since the POMINO v1.1 algorithm uses MODIS AOD to adjust model AOD, it only

416   uses the CALIOP aerosol extinction profile shape to adjust the modeled shape (Eqs. 1

417   and 2). Figures 4b and 4b show the vertical shapes of aerosol extinction, averaged

418   across all profiles in each season over Northern East China and Northwest China,

419   respectively. Over Northern East China (Fig. 4b), GEOS-Chem underestimates the

420   CALIOP values above 1 km by 52–71%. This underestimate leads to a lower ALH,

421   consistent with the finding by van Donkelaar et al. (2013) and Lin et al. (2014b). Over

422   Northwest China (Fig. 5b), the model also underestimates the CALIOP values above 1

423   km by 50–62%. These results imply the importance of correcting the modeled aerosol

424   vertical shape prior to cloud and NO_2 retrievals.

425   **4. Effects of aerosol vertical profile improvement on cloud retrieval in 2012**

426   Figure 6a, b shows the monthly average ALH and cloud top height (CTH,

427   corresponding to cloud pressure, CP) over Northern East China and Northwest China

428   in 2012. In order to discuss the CTH, only cloudy days are analyzed here, by excluding

17

429   days with zero cloud fraction (CF = 0, clear-sky cases) in POMINO. Although "clear

430   sky" is used sometimes in the literature to represent low cloud coverage (e.g., CF < 0.2

431   or CRF < 0.5, Boersma et al., 2011; Chimot et al., 2016), here it strictly means CF = 0

432   while "cloudy sky" means CF > 0. About 62.7% of days contain non-zero fractions of

433   clouds over Northern East China, and the number is 59.1% for Northwest China. The

434   CF changes from POMINO to POMINO v1.1 (i.e., after aerosol vertical profile

435   adjustment) are negligible (within $\pm0.5\%$, not shown) due to the same values of AOD

436   and SSA used in both products. This is because overall CF is mostly driven by the

437   continuum reflectance at 475 nm (mainly determined by AOD and surface reflectance,

438   which remain unchanged), which is independent of aerosol profile but CTH is driven

439   by the O_2-O_2 SCD, which is itself impacted by ALH.

440   Figure 6a, b shows that over the two regions, the CTH varies notably from one month

441   to another, whereas the ALH is much more stable across the months. Over Northern

442   East China, the ALH increases by 0.52 km from POMINO (orange dashed line) to

443   POMINO v1.1 (orange solid line) due to the CALIOP-based monthly climatological

444   adjustment. The increase in ALH means a stronger "shielding" effect of aerosols on the

445   O_2-O_2 absorbing dimer, which, in turn, results in a reduced CTH by 0.69 km on average.

446   For POMINO over Northern East China (Fig. 6a), the retrieved clouds usually extend

447   above the aerosol layer, i.e., the CTH (grey dashed line) is much larger than the ALH

448   (orange dashed line). Using the CALIOP climatology in POMINO v1.1 results in the

449   ALH higher than the CTH in fall and winter. The more elevated ALH is consistent with

450   the finding of Jethva et al. (2016) that a significant amount of absorbing aerosols resides

451   above clouds over Northern East China based on 11-year (2004–2015) OMI near-UV

452   observations.

453   The CTH in Northwest China is much lower than in Northern East China (Fig. 6a versus

454   7b). This is because the dominant type of actual clouds is (optically thin) cirrus over

18

455　western China (Wang et al., 2014), which is interpreted by the O_2-O_2 cloud retrieval

456　algorithm as reduced CTH (with cloud base from the ground). The reduction in CTH

457　from POMINO to POMINO v1.1 over Northwest China is also smaller than the

458　reduction over Northern East China, albeit with a similar enhancement in ALH, due to

459　lower aerosol loadings (Fig. 6c versus 6d).

460　Figure 7g,h presents the relative change in CP from POMINO to POMINO v1.1 as a

461　function of AOD (binned at an interval of 0.1) and changes in ALH from POMINO to

462　POMINO v1.1 (ΔALH, binned every 0.2 km) across all pixels in 2012 over Northern

463　East China. Results are separated for low cloud fraction (CF < 0.05 in POMINO, Fig.

464　7g) and modest cloud fraction (0.2 < CF < 0.3, Fig. 7h). The median of the CP changes

465　for pixels within each AOD and ΔALH bin is shown. Figure 7e,f presents the

466　corresponding numbers of occurrence under the two cloud conditions.

467　Figure 7 shows that over Northern East China, the increase in ALH is typically within

468　0.6 km for the case of CF < 0.05 (Fig. 7e), and the corresponding increase in CP is

469　within 6% (Fig. 7g). In this case, the average CTH (2.95 km in POMINO versus 1.58

470　km in POMINO v1.1) becomes much lower than the average ALH (1.06 km in

471　POMINO versus 1.98 km in POMINO v1.1). For the case with CF between 0.2 and 0.3,

472　the increase in ALH is within 1.2 km for most scenes (Fig. 7f), which leads to a CP

473　change of 2% (Fig. 7h), much smaller than the CP change for CF < 0.05 (Fig. 7g). This

474　is partly because the larger the CF is, the smaller a change in CF is required to

475　compensate for the ΔALH in the O_2-O_2 cloud retrieval algorithm. Furthermore, with

476　0.2 < CF < 0.3, the mean value of CTH is much higher than ALH in both POMINO

477　(2.76 km for CTH versus 1.13km for ALH) and POMINO v1.1 (2.60km for CTH versus

478　2.09 km for ALH), thus a large portion of clouds are above aerosols so that the change

479　in CP is less sensitive to ΔALH. We find that the summertime data contribute the

480　highest portion (36.5%) to the occurrences for 0.2 < CF < 0.3.

19

481 For Northwest China (not shown), the dependence of CP changes to AOD and ΔALH

482 is similar to that for Northern East China. In particular, the CP change is within 10%

483 on average for the case of CF < 0.05 and 1.5% for the case of 0.2 < CF < 0.3.

5. Effects of aerosol vertical profile improvement on NO_2 retrieval in 2012

485 Figure 7a presents the percentage changes in clear-sky NO_2 VCD from POMINO to

486 POMINO v1.1 as a function of binned AOD and ΔALH over Northern East China. Here,

487 clear-sky pixels are chosen based on CF = 0 in POMINO. In any AOD bin, an increase

488 in ΔALH leads to an enhancement in NO_2. And for any ΔALH, the change in VCD is

489 greater (smaller) when AOD becomes larger (smaller), which indicates that the NO_2

490 retrieval is more sensitive to ALH in high aerosol loading cases. Clearly, the change in

491 NO_2 is not a linear function of AOD and ΔALH.

492 For cloudy scenes (Fig. 7b,c, cloud data are based on POMINO), the change in NO_2

493 VCD is less sensitive to AOD and ΔALH. This is because the existence of clouds limits

494 the optical effect of aerosols on tropospheric NO_2. Figure 6a presents the nitrogen layer

495 height (NLH, defined as the average height of model simulated NO_2 weighted by its

496 volume mixing ratio in each layer) in comparison to the ALH and CLH over Northern

497 East China. The figure shows that the POMINO v1.1 CTH is higher than the NLH in

498 all months and higher than the ALH in warm months, which means a "shielding" effect

499 on both NO_2 and aerosols.

500 Over Northwest China (not shown), the changes in clear-sky NO_2 VCD are within 9%

501 for most cases, which are much smaller than over Eastern China (within 18%). This is

502 because the NLH is much higher than the CLH and ALH (Fig. 6b) in absence of surface

503 anthropogenic emissions.

20

504   We convert the valid pixels into monthly mean Level-3 values datasets on a 0.25° long.

505   × 0.25° lat. grid. Figure 8a,b compares the seasonal spatial variations of NO_2 VCD in

506   POMINO v1.1 and POMINO in 2012. In both products, NO_2 peaks in winter due to the

507   longest lifetime and highest anthropogenic emissions (Lin, 2012). NO_2 also reaches a

508   maximum over Northern East China as a result of substantial anthropogenic sources.

509   From POMINO to POMINO v1.1, the NO_2 VCD increases by 3.4% (-67.5–41.7%) in

510   spring for the domain average (range), 3.0% (-59.5–34.4%) in summer, 4.6% (-15.3–

511   39.6%) in fall and 5.3% (-68.4–49.3%) in winter. The NO_2 change is highly dependent

512   on the location and season. The increase over Northern East China is largest in winter,

513   wherein the positive value for ΔALH implies that elevated aerosol layers "shield" the

514   NO_2 absorption.

515   6. Evaluating satellite products using MAX-DOAS data

516   We use MAX-DOAS data, after cloud screening (Sect. 2.4), to evaluate DOMNO v2,

517   QA4ECV, POMINO and POMINO v1.1. The scatterplots in Fig. 9a-d compare the NO_2

518   VCDs from 162 OMI pixels on 49 days with their MAX-DOAS counterparts. Different

519   colors differentiate the seasons. The high values of NO_2 VCD (> 30 × 10^{15} molec. cm⁻

520   ^{2}) occur mainly in fall (blue) and winter (black). POMINO v1.1 and POMINO capture

521   the day-to-day variability of MAX-DOAS data, i.e., R^2 = 0.804 and 0.799, respectively.

522   The normalized mean bias (NMB) of POMINO v1.1 relative to MAX-DOAS data (-

523   3.4%) is smaller than the NMB of POMINO (-9.6%). Also, the reduced major axis

524   (RMA) regression shows that the slope for POMINO v1.1 (0.95) is closer to unity than

525   the slope for POMINO (0.78). When all OMI pixels in a day are averaged (Fig. 9e,f),

526   the correlation across the total of 49 days further increase for both POMINO v1.1 (R^2

527   = 0.89) and POMINO (R^2 = 0.86), whereas POMINO v1.1 still has a lower NMB (-

528   3.7%) and better slope (0.96) than POMINO (-10.4% and 0.82, respectively). These

21

529 results suggest that correcting aerosol vertical profiles, at least on a climatology basis,

530 already leads to a significant improved NO_2 retrieval from OMI.

531 Figure 9 shows that DOMINO v2 is correlated with MAX-DOAS ($R^2 = 0.68$ in Fig. 9c

532 and 0.75 in Fig. 9g) but not as strong as POMINO and POMINO v1.1 for all days. The

533 discrepancy between DOMINO v2 and MAX-DOAS is particularly large for very high

534 NO_2 values (> 70 $\times$ 10^{15} molec. cm^{-2}). ==The R^2 for QA4ECV (0.75 in Fig. 9d and 0.82==

535 ==in Fig. 9h) is slightly better than DOMINO, but the NMB is higher (-22.0% and -22.7%)==

536 ==and the slope drops to 0.66.== These results are consistent with the finding of Lin et al.

537 (2014b, 2015) that explicitly including aerosol optical effects improves the NO_2

538 retrieval.

539 Table 2 further shows the comparison statistics for 27 haze days. The haze days are

540 determined when both the ground meteorological station data and MODIS/Aqua

541 corrected reflectance (true color) data indicate a haze day. The table also lists AOD,

542 SSA, CF and MAX-DOAS NO_2 VCD, as averaged over all haze days. A large amount

543 of absorbing aerosols occurs on these haze days (AOD = 1.13, SSA = 0.90). The

544 average MAX-DOAS NO_2 VCD reaches 51.92 $\times$ 10^{15} molec. cm^{-2}. Among the four

545 satellite products, POMINO v1.1 has the highest R^2 (0.76) and the lowest bias (4.4%)

546 with respect to MAX-DOAS, whereas DOMINO v2 and QA4ECV reproduce the

547 variability to a limited extent ($R^2 = 0.38$ and 0.34, respectively). This is consistent with

548 the previous finding that the accuracy of DOMINO v2 is reduced for polluted, aerosol-

549 loaded scenes (Boersma et al., 2011; Chimot et al., 2016; Kanaya et al., 2014; Lin et

550 al., 2014b).

551 Table 3 shows the comparison statistics for 36 cloud-free days (CF = 0 in POMINO,

552 and AOD = 0.60 on average). Here, POMINO v1.1, POMINO and DONIMO v2 do not

553 show large differences in R^2 (0.53–0.56) and NMB (20.8–29.4%) with respect to MAX-

554 DOAS. QA4ECV has a higher R^2 (0.63) and a lower NMB (-5.83%), presumably

22

批注 [Microsof7]: Add discussion about QA4ECV product.

555 reflecting the improvements in this (EU-) consortium approach, at least in mostly cloud-
556 free situations. However, the R^2 values for POMINO and POMINO v1.1 are much
557 smaller than the R^2 values in haze days, whereas the opposite changes are true for
558 DOMINO v2 and QA4ECV. Thus, for this limited set of data, the changes from
559 DOMINO v2 and QA4ECV to POMINO and POMINO v1.1 mainly reflect the
560 improved aerosol treatment in hazy scenes. Further research may use additional MAX-
561 DOAS datasets to evaluate the satellite products more systematically.

562 **7. Conclusions**

563 This paper improves upon our previous POMINO algorithm (Lin et al., 2015) to retrieve
564 the tropospheric NO_2 VCDs from OMI, by compiling a 9-year (2007–2015) CALIOP
565 monthly climatology of aerosol vertical extinction profiles to adjust GEOS-Chem
566 aerosol profiles used in the NO_2 retrieval process. The improved algorithm is referred
567 to as POMINO v1.1. Compared to monthly climatological CALIOP data over China,
568 GEOS-Chem simulations tend to underestimate the aerosol extinction above 1 km, as
569 characterized by an underestimate in ALH by 300–600 m (seasonal and location
570 dependent). Such a bias is corrected in POMINO v1.1 by dividing, for any month and
571 grid cell, the CALIOP monthly climatological profile by the model climatological
572 profile to obtain a scaling profile and then applying the scaling profile to model data in
573 all days of that month in all years.

574 The aerosol extinction profile correction leads to an insignificant change in CF from
575 POMINO to POMINO v1.1, since the AOD and surface reflectance are unchanged. In
576 contrast, the correction results in a notably increase in CP (i.e., a decrease in CTH), due
577 to lifting of aerosol layers. The CP changes are generally within 6% for scenes with low
578 cloud fraction (CF < 0.05 in POMINO), and within 2% for scenes with modest cloud
579 fraction (0.2 < CF < 0.3 in POMINO).

23

580   The NO_2 VCDs increase from POMINO to POMINO v1.1 in most cases due to lifting

581   of aerosol layers that enhances the "shielding" of NO_2 absorption. The NO_2 VCD

582   increases by 3.4% (-67.5–41.7%) in spring for the domain average (range), 3.0% (-

583   59.5–34.4%) in summer, 4.6% (-15.3–39.6%) in fall and 5.3% (-68.4–49.3%) in winter.

584   The NO_2 changes highly season and location dependent, and are most significant for

585   wintertime Northern East China.

586   Further comparisons with independent MAX-DOAS NO_2 VCD data for 162 OMI

587   pixels in 49 days show good performance of both POMINO v1.1 and POMINO in

588   capturing the day-to-day variation of NO_2 (R^2=0.80, n=162), compared to DOMINO

589   v2 (R^2=0.67) and the new QA4ECV product (R^2=0.75). The NMB is smaller in

590   POMINO v1.1 (-3.4%) than in POMINO (-9.6%), with a slightly better slope (0.804

591   versus 0.784). On hazy days with high aerosol loadings (AOD = 1.13 on average),

592   POMINO v1.1 has the highest R^2 (0.76) and the lowest bias (4.4%) whereas DOMINO

593   and QA4ECV have difficulty in reproducing the day-to-day variability in MAX-DOAS

594   NO_2 measurements (R^2 = 0.38 and 0.34, respectively). The four products show small

595   differences in R^2 on clear-sky days (CF = 0 in POMINO, AOD = 0.60 on average),

596   among which QA4ECV shows a highest R^2 (0.63) and lowest NMB (-5.83%),

597   presumably reflecting the improvements in less polluted place such as Europe and the

598   US. Thus the explicit aerosol treatment (in POMINO and POMINO v1.1) and the

599   aerosol vertical profile correction (in POMINO v1.1) improves the NO_2 retrieval

600   especially in hazy cases.

601   The POMINO v1.1 algorithm is a core step towards our next public release of data

602   product, POMINO v2. This new release will contain a few additional updates, including

603   but not limited to using MODIS Collection 6 Merged 10-km Level-2 AOD data that

604   combine the Dark Target (Levy et al., 2013) and Deep Blue (Sayer et al., 2014) products,

605   as well as MODIS MCD43C2 Collection 6 daily BRDF data. Meanwhile, the POMINO

批注 [Microsof8]: Clarify POMINO v1.1 won't be our released version.

24

606 algorithm framework is being applied to the recently launched TropOMI instrument
607 that provides NO_2 information at a much higher spatial resolution (3.5 x 7 km^2). A
608 modified algorithm can also be used to retrieve sulfur dioxide, formaldehyde and other
609 trace gases from TropOMI, for which purposes our algorithm will be available to the
610 community on a collaborative basis. Future research can correct the SSA and NO_2
611 vertical profile to further improve the retrieval algorithm, and can use more
612 comprehensive independent data to evaluate the resulting satellite products.

617 **Appendix A: Introduction to the QA4ECV product**

618 The QA4ECV NO_2 product (http://www.qa4ecv.eu/) builds on a (EU-) consortium
619 approach to retrieve NO_2 from GOME, SCIAMACHY, GOME-2, and OMI. The main
620 contributions are provided by BIRA-IASB, the University of Bremen (IUP), MPIC,
621 KNMI, and Wageningen University. Uncertainties in spectral fitting for NO_2 SCDs and
622 in AMF calculations were evaluated by Zara et al. (2018) and Lorente et al. (2017),
623 respectively. QA4ECV contains improved SCD NO_2 data (Zara et al., 2018). Lorente
624 et al., (2017) showed that across the above algorithms, there a structural uncertainty by
625 42% in the NO_2 AMF calculation over polluted areas. By comparing to our POMINO
626 product, Lorente et al. also showed that the choice of aerosol correction may introduce
627 an additional uncertainty by up to 50% for situations with high polluted cases,
628 consistent with Lin et al. (2014b, 2015) and the findings here. For a complete
629 description of the QA4ECV algorithm improvements, and quality assurance, please see
630 Boersma et al. (2018).

25

Appendix B: Constructing the CALIOP monthly climatology of aerosol

extinction vertical profile

Our use the all-sky Level-2 CALIOP data to construct the Level-3 monthly climatology. We choose the all-sky product instead of clear-sky data, since previous studies indicate that the climatological aerosol extinction profiles are affected insignificantly by the presence of clouds (Koffi et al., 2012; Winker et al., 2013). As we use this climatological data to adjust GEOS-Chem results, choosing all-sky data improves consistency with the model simulation when doing the daily correction.

To select valid pixels, we follow the data quality criteria by Winker et al., (2013) and Amiridis et al., (2015). Only the pixels with Cloud Aerosol Discrimination (CAD) scores between -20 and -100 with extinction Quality Control (QC) flag valued at 0, 1, 18, and 16 are selected. We further discard samples with an extinction uncertainty of 99.9 km^{-1}, which is indicative of unreliable retrieval. We only accept extinction values falling in the range from 0.0 to 1.25, according to CALIOP observation thresholds. Previous studies showed that weakly scattering edges of icy clouds are sometimes misclassified as aerosols (Winker et al., 2013). To eliminate contamination from icy clouds we exclude the aerosol layers above the cloud layer (with layer-top temperature below 0 ℃) when both of them are above 4km (Winker et al., 2013).

After the pixel-based screening, we aggregate the CALIOP data at the model grid (0.667° long. x 0.5° lat.) and vertical resolution (47 layers, with 36 layers or so in the troposphere). For each grid cell, we choose the CALIOP pixels within 1.5° of the grid cell center. CALIOP Level-2 data are always presented at the fixed 399 altitudes above sea level. To account for the difference in surface elevation between a CALIOP pixel and the respective model grid cell, we convert the altitude of the pixel to a height above the ground, by using the surface elevation data provided in CALIOP. We then average horizontally and vertically the profiles of all pixels within one model grid cell and layer.

657 We do the regridding day-by-day for all grid cells to ensure that GEOS-Chem and
658 CALIOP extinction profiles are coincident spatially and temporally. Finally, we
659 compile a monthly climatological dataset by averaging over 2007–2015.

660 Figure A1 shows the number of aerosol extinction profiles in each grid cell and 12 x 9
661 = 108 months that are used to compile the CALIOP climatology, both before and after
662 data screening. Table A1 presents additional information on monthly and yearly bases.
663 On average, there are 165 and 47 aerosol extinction profiles per month per grid cell
664 before and after screening, respectively. In the final 9-year monthly climatology, each
665 grid cell has about 420 aerosol extinction profiles on average, about 28% of the prior-
666 screening profiles. Figure A1 shows that the number of valid profiles decreases sharply
667 over the Tibet Plateau and at higher latitudes (> 43 ° N) due to complex terrain and
668 icy/snowy ground.

669 As discussed above, we choose the CALIOP pixels within 1.5° of a grid cell center.
670 We test this choice by examining the aerosol layer height (ALH) produced for that grid
671 cell. The ALH is defined as the extinction-weighted height of aerosols (see Eq. A1,
672 where n denotes the number of tropospheric layers, ε_i the aerosol extinction at layer
673 i, and H_i the layer center height above the ground). We find that choosing pixels
674 within 1.0° of a grid cell center leads to a nosier horizontal distribution of ALH, owing
675 to the small footprint of CALIOP. On the other hand, choosing 2.0° leads to a too
676 smooth spatial gradient of ALH with local characteristics of aerosol vertical
677 distributions are largely lost. We thus decide that 1.5 ° is a good balance between
678 noise and smoothness.

679 $\text{ALH} = \dfrac{\sum_{i=1}^{i=n} \varepsilon_i H_i}{\sum_{i=1}^{i=n} \varepsilon_i}$ (A1)

680 Certain grid cells do not contain sufficient valid observations for some months of the
681 climatological dataset. We fill in missing monthly values of a grid cell using valid data

682   in the surrounding 5 x 5 = 25 grid cells (within ~ 100 km). If the 25 grid cells do not

683   have enough valid data, we use those in the surrounding 7 x 7 = 49 grid cells (within ~

684   150 km). A similar procedure is used by Lin et al. (2014b, 2015) to fill in missing values

685   in the gridded MODIS AOD dataset.

686   For each grid cell in each month, we further correct singular values in the vertical profile.

687   In a month, if a grid cell i has an ALH outside mean$\pm 1 \sigma$ of its surrounding 25 or 49

688   grid cells, we select i's surrounding grid cell j whose ALH is the median of i's

689   surrounding grid cells, and use j's profile to replace i's. Whether 25 or 49 surrounding

690   grid cells are chosen depends on the number of valid pixels shown in Fig. A1b. If the

691   number of valid pixels in i is below mean–1 σ of all grid cells in the whole domain,

692   which is often the case for Tibetan grid cells, we use i's surrounding 49 grid cells;

693   otherwise we use i's surrounding 25 grid cells.

694   **Appendix C. Comparing our and NASA's CALIOP monthly climatology**

695   We compare our gridded climatological profiles to NASA CALIOP Version 3 Level-3

696   all-sky monthly profiles at 532 nm (Winker et al., 2013). The NASA Level-3 data has

697   a horizontal resolution of 2 ° lat. × 5 ° lon. and a vertical resolution of 60 m (from -

698   0.5 to 12 km above sea level). We combine NASA monthly data over 2007–2015 to

699   construct a monthly climatology for comparison with our own compilation. We only

700   choose aerosol extinction data in the troposphere with error less than 0.15 (the valid

701   range given in the CALIOP dataset). If the number of valid monthly profiles in a grid

702   cell is less than five (i.e., for the same month in five out of the nine years), then we

703   exclude data in that grid cell; see the dark gray grid cells in Fig. 2c.

704   Several methodological differences exist between generating our and NASA CALIOP

705   datasets. First, the two datasets have different horizontal resolutions. Also, we sample

706   all valid CALIOP pixels within 1.5º of a grid cell center, whereas the NASA dataset

707 samples all valid pixels within a grid cell. Besides, our CALIOP dataset involves

708 several steps of horizontal interpolation, for purposes of subsequent cloud and NO_2

709 retrievals, which is not done in the NASA dataset. In addition, we match CALIOP data

710 vertically to the GEOS-Chem vertical resolution, whereas the NASA dataset maintains

711 the original resolution.

712 Figure 2c shows the spatial distribution of ALH in all seasons based on NASA CALIOP

713 Level-3 all-sky monthly climatology. The horizontal resolution of NASA data is much

714 coarser than ours; and NASA data are largely missing over the southwest with complex

715 terrains. We choose to focus on the comparison over East China (the black box in Fig.

716 1a). Over East China, the two climatology datasets generally exhibit similar spatial

717 patterns of ALH in all seasons (Fig. 2a, c). The NASA dataset suggests higher ALHs

718 than ours over Eastern China, especially in summer, due mainly to differences in the

719 sampling and regridding processes. Figure 3c further compares the monthly variation

720 of ALH between our (black line with error bars) and NASA (blue filled triangles)

721 datasets averaged over East China. The two datasets are consistent in almost all months,

722 indicating that their regional differences are largely smoothed out by spatial averaging.

723 **References**

724 Acarreta, J. R., De Haan, J. F. and Stammes, P.: Cloud pressure retrieval using the O_2

725 -O_2 absorption band at 477 nm, J. Geophys. Res., 109(D5), D05204,

726 doi:10.1029/2003JD003915, 2004.

727 Amiridis, V., Marinou, E., Tsekeri, A., Wandinger, U., Schwarz, A., Giannakaki, E.,

728 Mamouri, R., Kokkalis, P., Binietoglou, I., Solomos, S., Herekakis, T., Kazadzis, S.,

729 Gerasopoulos, E., Proestakis, E., Kottas, M., Balis, D., Papayannis, A., Kontoes, C.,

730 Kourtidis, K., Papagiannopoulos, N., Mona, L., Pappalardo, G., Le Rille, O. and

731 Ansmann, A.: LIVAS: a 3-D multi-wavelength aerosol/cloud database based on

732 CALIPSO and EARLINET, Atmos. Chem. Phys., 15(13), 7127–7153,

733 doi:10.5194/acp-15-7127-2015, 2015.

734 Belmonte Rivas, M., Veefkind, P., Boersma, F., Levelt, P., Eskes, H. and Gille, J.:

735 Intercomparison of daytime stratospheric NO_2 satellite retrievals and model

736 simulations, Atmos. Meas. Tech., 7(7), 2203–2225, doi:10.5194/amt-7-2203-2014,

737 2014.

738 Boersma, K. F., Eskes, H. J. and Brinksma, E. J.: Error analysis for tropospheric NO_2

739 retrieval from space, J. Geophys. Res. Atmos., 109(D4), n/a-n/a,

740 doi:10.1029/2003JD003962, 2004.

741 Boersma, K. F., Eskes, H. J., Veefkind, J. P., Brinksma, E. J., van der A, R. J., Sneep,

742 M., van den Oord, G. H. J., Levelt, P. F., Stammes, P., Gleason, J. F. and Bucsela, E.

743 J.: Near-real time retrieval of tropospheric NO_2 from OMI, Atmos. Chem. Phys., 7(8),

744 2103–2118, doi:10.5194/acp-7-2103-2007, 2007.

745 Boersma, K. F., Eskes, H. J., Dirksen, R. J., van der A, R. J., Veefkind, J. P.,

746 Stammes, P., Huijnen, V., Kleipool, Q. L., Sneep, M., Claas, J., Leitão, J., Richter, A.,

747 Zhou, Y. and Brunner, D.: An improved tropospheric NO_2 column retrieval algorithm

748 for the Ozone Monitoring Instrument, Atmos. Meas. Tech., 4(9), 1905–1928,

749 doi:10.5194/amt-4-1905-2011, 2011.

750 Boersma, K.F., Eskes, H. J., Richter, A., De Smedt, I., Lorente, A., Beirle, S., van

751 Geffen, J. H. G. M., Zara, M., Peters, E., Van Roozendael, M., Wagner, T., Maasakkers,

752 J. D., van der A, R. J., Nightingale, J., De Rudder, A., Irie, H., and Pinardi, G.:

753 Improving algorithms and uncertainty estimates for satellite NO_2 retrievals: Results

754 from the Quality Assurance for Essential Climate Variables (QA4ECV) project, amt-

755 2018-200, submitted, 2018.

756 Bucsela, E. J., Celarier, E. A., Wenig, M. O., Gleason, J. F., Veefkind, J. P., Boersma,

757 K. F. and Brinksma, E. J.: Algorithm for NO_2 vertical column retrieval from the

758 ozone monitoring instrument, IEEE Trans. Geosci. Remote Sens., 44(5), 1245–1258,

759 doi:10.1109/TGRS.2005.863715, 2006.

760 Bucsela, E. J., Krotkov, N. A., Celarier, E. A., Lamsal, L. N., Swartz, W. H., Bhartia,

761 P. K., Boersma, K. F., Veefkind, J. P., Gleason, J. F. and Pickering, K. E.: A new

762 stratospheric and tropospheric NO_2 retrieval algorithm for nadir-viewing satellite

763 instruments: applications to OMI, Atmos. Meas. Tech., 6(10), 2607–2626,

764 doi:10.5194/amt-6-2607-2013, 2013.

765 Castellanos, P., Boersma, K. F. and van der Werf, G. R.: Satellite observations

766 indicate substantial spatiotemporal variability in biomass burning NO_X emission

767 factors for South America, Atmos. Chem. Phys., 14(8), 3929–3943, doi:10.5194/acp-

768 14-3929-2014, 2014.

769 Castellanos, P., Boersma, K. F., Torres, O. and de Haan, J. F.: OMI tropospheric NO_2

770 air mass factors over South America: effects of biomass burning aerosols, Atmos.

771 Meas. Tech., 8(9), 3831–3849, doi:10.5194/amt-8-3831-2015, 2015.

772 Chazette, P., Raut, J.-C., Dulac, F., Berthier, S., Kim, S.-W., Royer, P., Sanak, J.,

773 Loaëc, S. and Grigaut-Desbrosses, H.: Simultaneous observations of lower

774 tropospheric continental aerosols with a ground-based, an airborne, and the

775 spaceborne CALIOP lidar system, J. Geophys. Res., 115(D4), D00H31,

776 doi:10.1029/2009JD012341, 2010.

777 Chimot, J., Vlemmix, T., Veefkind, J. P., de Haan, J. F. and Levelt, P. F.: Impact of

778 aerosols on the OMI tropospheric NO_2 retrievals over industrialized regions: how

779 accurate is the aerosol correction of cloud-free scenes via a simple cloud model?,

780 Atmos. Meas. Tech., 9(2), 359–382, doi:10.5194/amt-9-359-2016, 2016.

31

781   Clémer, K., Van Roozendael, M., Fayt, C., Hendrick, F., Hermans, C., Pinardi, G.,

782   Spurr, R., Wang, P. and De Mazière, M.: Multiple wavelength retrieval of

783   tropospheric aerosol optical properties from MAX-DOAS measurements in Beijing,

784   Atmos. Meas. Tech., 3(4), 863–878, doi:10.5194/amt-3-863-2010, 2010.

785   Cui, Y., Lin, J., Song, C., Liu, M., Yan, Y., Xu, Y. and Huang, B.: Rapid growth in

786   nitrogen dioxide pollution over Western China, 2005–2013, Atmos. Chem. Phys.,

787   16(10), 6207–6221, doi:10.5194/acp-16-6207-2016, 2016.

788   Dirksen, R. J., Boersma, K. F., Eskes, H. J., Ionov, D. V., Bucsela, E. J., Levelt, P. F.

789   and Kelder, H. M.: Evaluation of stratospheric NO_2 retrieved from the Ozone

790   Monitoring Instrument: Intercomparison, diurnal cycle, and trending, J. Geophys.

791   Res., 116(D8), D08305, doi:10.1029/2010JD014943, 2011.

792   van Geffen, J. H. G. M., Boersma, K. F., Van Roozendael, M., Hendrick, F., Mahieu,

793   E., De Smedt, I., Sneep, M. and Veefkind, J. P.: Improved spectral fitting of nitrogen

794   dioxide from OMI in the 405–465 nm window, Atmos. Meas. Tech., 8(4), 1685–

795   1699, doi:10.5194/amt-8-1685-2015, 2015.

796   Gielen, C., Van Roozendael, M., Hendrick, F., Pinardi, G., Vlemmix, T., De Bock,

797   V., De Backer, H., Fayt, C., Hermans, C., Gillotay, D. and Wang, P.: A simple and

798   versatile cloud-screening method for MAX-DOAS retrievals, Atmos. Meas. Tech.,

799   7(10), 3509–3527, doi:10.5194/amt-7-3509-2014, 2014.

800   Hendrick, F., Muller, J. F., Clemer, K., Wang, P., De Maziere, M., Fayt, C., Gielen,

801   C., Hermans, C., Ma, J. Z., Pinardi, G., Stavrakou, T., Vlemmix, T., and Van

802   Roozendael, M.: Four years of ground-based MAX-DOAS observations of HONO

803   and NO_2 in the Beijing area, Atmospheric Chemistry and Physics, 14, 765-781,

804   10.5194/acp-14-765-2014, 2014.

805   Huang, Z., Huang, J., Bi, J., Wang, G., Wang, W., Fu, Q., Li, Z., Tsay, S.-C. and Shi,

806   J.: Dust aerosol vertical structure measurements using three MPL lidars during 2008

807   China-U.S. joint dust field experiment, J. Geophys. Res. Atmos., 115(D7), n/a-n/a,

808   doi:10.1029/2009JD013273, 2010.

809   Irie, H., Boersma, K. F., Kanaya, Y., Takashima, H., Pan, X. and Wang, Z. F.:

810   Quantitative bias estimates for tropospheric NO_2 columns retrieved from

811   SCIAMACHY, OMI, and GOME-2 using a common standard for East Asia, Atmos.

812   Meas. Tech., 5(10), 2403–2411, doi:10.5194/amt-5-2403-2012, 2012.

813   Jethva, H., Torres, O., and Ahn, C.: A ten-year global record of absorbing aerosols

814   above clouds from OMI's near-UV observations, in: Remote Sensing of the Atmosphere,

815   Clouds, and Precipitation Vi, edited by: Im, E., Kumar, R., and Yang, S., Proceedings

816   of SPIE, 2016.

817   Johnson, M. S., Meskhidze, N. and Praju Kiliyanpilakkil, V.: A global comparison of

818   GEOS-Chem-predicted and remotely-sensed mineral dust aerosol optical depth and

819   extinction profiles, J. Adv. Model. Earth Syst., 4(3), M07001,

820   doi:10.1029/2011MS000109, 2012.

821   Kacenelenbogen, M., Redemann, J., Vaughan, M. A., Omar, A. H., Russell, P. B.,

822   Burton, S., Rogers, R. R., Ferrare, R. A. and Hostetler, C. A.: An evaluation of

823   CALIOP/CALIPSO's aerosol-above-cloud detection and retrieval capability over

824   North America, J. Geophys. Res. Atmos., 119(1), 230–244,

825   doi:10.1002/2013JD020178, 2014.

826   Kanaya, Y., Irie, H., Takashima, H., Iwabuchi, H., Akimoto, H., Sudo, K., Gu, M.,

827   Chong, J., Kim, Y. J., Lee, H., Li, A., Si, F., Xu, J., Xie, P.-H., Liu, W.-Q., Dzhola,

828   A., Postylyakov, O., Ivanov, V., Grechko, E., Terpugova, S. and Panchenko, M.:

829   Long-term MAX-DOAS network observations of NO_2 in Russia and Asia

830 (MADRAS) during the period 2007-2012: instrumentation, elucidation of

831 climatology, and comparisons with OMI satellite observations and global model

832 simulations, Atmos. Chem. Phys., 14(15), 7909–7927, doi:10.5194/acp-14-7909-

833 2014, 2014.

834 Kim, S.-W., Heckel, A., Frost, G. J., Richter, A., Gleason, J., Burrows, J. P., McKeen,

835 S., Hsie, E.-Y., Granier, C. and Trainer, M.: NO_2 columns in the western United

836 States observed from space and simulated by a regional chemistry model and their

837 implications for NO_x emissions, J. Geophys. Res., 114(D11), D11301,

838 doi:10.1029/2008JD011343, 2009.

839 Koffi, B., Schulz, M., Bréon, F.-M., Griesfeller, J., Winker, D., Balkanski, Y., Bauer,

840 S., Berntsen, T., Chin, M., Collins, W. D., Dentener, F., Diehl, T., Easter, R., Ghan,

841 S., Ginoux, P., Gong, S., Horowitz, L. W., Iversen, T., Kirkevåg, A., Koch, D., Krol,

842 M., Myhre, G., Stier, P. and Takemura, T.: Application of the CALIOP layer product

843 to evaluate the vertical distribution of aerosols estimated by global models: AeroCom

844 phase I results, J. Geophys. Res. Atmos., 117(D10), n/a-n/a,

845 doi:10.1029/2011JD016858, 2012.

846 Leitão, J., Richter, A., Vrekoussis, M., Kokhanovsky, A., Zhang, Q. J., Beekmann, M.

847 and Burrows, J. P.: On the improvement of NO_2 satellite retrievals – aerosol impact

848 on the airmass factors, Atmos. Meas. Tech., 3(2), 475–493, doi:10.5194/amt-3-475-

849 2010, 2010.

850 Lerot, C., Stavrakou, T., De Smedt, I., Müller, J.-F. and Van Roozendael, M.: Glyoxal

851 vertical columns from GOME-2 backscattered light measurements and comparisons

852 with a global model, Atmos. Chem. Phys., 10(24), 12059–12072, doi:10.5194/acp-10-

853 12059-2010, 2010.

854 Levy, R. C., Mattoo, S., Munchak, L. A., Remer, L. A., Sayer, A. M., Patadia, F. and
855 Hsu, N. C.: The Collection 6 MODIS aerosol products over land and ocean, Atmos.
856 Meas. Tech., 6(11), 2989–3034, doi:10.5194/amt-6-2989-2013, 2013.

857 Li, S., Yu, C., Chen, L., Tao, J., Letu, H., Ge, W., Si, Y. and Liu, Y.: Inter-
858 comparison of model-simulated and satellite-retrieved componental aerosol optical
859 depths in China, Atmos. Environ., 141, 320–332,
860 doi:https://doi.org/10.1016/j.atmosenv.2016.06.075, 2016.

861 Lin, J., Pan, D., Davis, S. J., Zhang, Q., He, K., Wang, C., Streets, D. G., Wuebbles,
862 D. J. and Guan, D.: China's international trade and air pollution in the United States,
863 Proc. Natl. Acad. Sci., 111(5), 1736–1741, doi:10.1073/pnas.1312860111, 2014a.

864 Lin, J.-T.: Satellite constraint for emissions of nitrogen oxides from anthropogenic,
865 lightning and soil sources over East China on a high-resolution grid, Atmos. Chem.
866 Phys., 12(6), 2881–2898, doi:10.5194/acp-12-2881-2012, 2012.

867 Lin, J.-T., McElroy, M. B. and Boersma, K. F.: Constraint of anthropogenic NO_X
868 emissions in China from different sectors: a new methodology using multiple satellite
869 retrievals, Atmos. Chem. Phys., 10(1), 63–78, doi:10.5194/acp-10-63-2010, 2010.

870 Lin, J.-T., Martin, R. V., Boersma, K. F., Sneep, M., Stammes, P., Spurr, R., Wang,
871 P., Van Roozendael, M., Clémer, K. and Irie, H.: Retrieving tropospheric nitrogen
872 dioxide from the Ozone Monitoring Instrument: effects of aerosols, surface
873 reflectance anisotropy, and vertical profile of nitrogen dioxide, Atmos. Chem. Phys.,
874 14(3), 1441–1461, doi:10.5194/acp-14-1441-2014, 2014b.

875 Lin, J.-T., Liu, M.-Y., Xin, J.-Y., Boersma, K. F., Spurr, R., Martin, R. and Zhang,
876 Q.: Influence of aerosols and surface reflectance on satellite NO_2 retrieval: seasonal
877 and spatial characteristics and implications for NO_x emission constraints, Atmos.
878 Chem. Phys., 15(19), 11217–11241, doi:10.5194/acp-15-11217-2015, 2015.

879   Lorente, A., Folkert Boersma, K., Yu, H., Dörner, S., Hilboll, A., Richter, A., Liu, M.,

880   Lamsal, L. N., Barkley, M., De Smedt, I., Van Roozendael, M., Wang, Y., Wagner,

881   T., Beirle, S., Lin, J.-T., Krotkov, N., Stammes, P., Wang, P., Eskes, H. J. and Krol,

882   M.: Structural uncertainty in air mass factor calculation for NO_2 and HCHO satellite

883   retrievals, Atmos. Meas. Tech., 10(3), 759–782, doi:10.5194/amt-10-759-2017, 2017.

884   Lucht, W., Schaaf, C. B. and Strahler, A. H.: An algorithm for the retrieval of albedo

885   from space using semiempirical BRDF models, IEEE Trans. Geosci. Remote Sens.,

886   38(2), 977–998, doi:10.1109/36.841980, 2000.

887   Ma, J. Z., Beirle, S., Jin, J. L., Shaiganfar, R., Yan, P. and Wagner, T.: Tropospheric

888   NO_2 vertical column densities over Beijing: results of the first three years of ground-

889   based MAX-DOAS measurements (2008-2011) and satellite validation, Atmos.

890   Chem. Phys., 13(3), 1547–1567, doi:10.5194/acp-13-1547-2013, 2013.

891   Ma, X. and Yu, F.: Seasonal variability of aerosol vertical profiles over east US and

892   west Europe: GEOS-Chem/APM simulation and comparison with CALIPSO

893   observations, Atmos. Res., 140–141, 28–37,

894   doi:https://doi.org/10.1016/j.atmosres.2014.01.001, 2014.

895   Martin, R. V.: An improved retrieval of tropospheric nitrogen dioxide from GOME, J.

896   Geophys. Res., 107(D20), 4437, doi:10.1029/2001JD001027, 2002.

897   Misra, A., Tripathi, S. N., Kaul, D. S. and Welton, E. J.: Study of MPLNET-Derived

898   Aerosol Climatology over Kanpur, India, and Validation of CALIPSO Level 2

899   Version 3 Backscatter and Extinction Products, J. Atmos. Ocean. Technol., 29(9),

900   1285–1294, doi:10.1175/JTECH-D-11-00162.1, 2012.

901   Miyazaki, K. and Eskes, H.: Constraints on surface NO_X emissions by assimilating

902   satellite observations of multiple species, Geophys. Res. Lett., 40(17), 4745–4750,

903   doi:10.1002/grl.50894, 2013.

36

904   Proestakis, E., Amiridis, V., Marinou, E., Georgoulias, A. K., Solomos, S., Kazadzis,

905   S., Chimot, J., Che, H., Alexandri, G., Binietoglou, I., Kourtidis, K. A., de Leeuw, G.

906   and van der A, R. J.: 9-year spatial and temporal evolution of desert dust aerosols over

907   South-East Asia as revealed by CALIOP, Atmos. Chem. Phys. Discuss., 1–35,

908   doi:10.5194/acp-2017-797, 2017.

909   Richter, A., Begoin, M., Hilboll, A. and Burrows, J. P.: An improved NO_2 retrieval

910   for the GOME-2 satellite instrument, Atmos. Meas. Tech., 4(6), 1147–1159,

911   doi:10.5194/amt-4-1147-2011, 2011.

912   Marchenko, S., Krotkov, N. A., Lamsal, L. N., Celarier, E. A., Swartz, W. H.,

913   and Bucsela, E. J.: Revising the slant column density retrieval of nitrogen dioxide

914   observed by the Ozone Monitoring Instrument, J. Geophys. Res. Atmos., 120(11),

915   5670–5692, doi:10.1002/2014JD022913, 2015.

916   Sareen, N., Schwier, A. N., Shapiro, E. L., Mitroo, D. and McNeill, V. F.: Secondary

917   organic material formed by methylglyoxal in aqueous aerosol mimics, Atmos. Chem.

918   Phys., 10(3), 997–1016, doi:10.5194/acp-10-997-2010, 2010.

919   Sayer, A. M., Munchak, L. A., Hsu, N. C., Levy, R. C., Bettenhausen, C. and Jeong,

920   M.-J.: MODIS Collection 6 aerosol products: Comparison between Aqua's e-Deep

921   Blue, Dark Target, and "merged" data sets, and usage recommendations, J. Geophys.

922   Res. Atmos., 119(24), 13,965-13,989, doi:10.1002/2014JD022453, 2014.

923   Schenkeveld, V. M. E., Jaross, G., Marchenko, S., Haffner, D., Kleipool, Q. L.,

924   Rozemeijer, N. C., Veefkind, J. P., and Levelt, P. F.: In-flight performance of the Ozone

925   Monitoring Instrument, Atmospheric Measurement Techniques, 10, 1957-1986,

926   10.5194/amt-10-1957-2017, 2017.

927   Stammes, P., Sneep, M., de Haan, J. F., Veefkind, J. P., Wang, P. and Levelt, P. F.:

928   Effective cloud fractions from the Ozone Monitoring Instrument: Theoretical

929   framework and validation, J. Geophys. Res., 113(D16), D16S38,

930   doi:10.1029/2007JD008820, 2008.

931   Stavrakou, T., Müller, J.-F., Bauwens, M., De Smedt, I., Lerot, C., Van Roozendael,

932   M., Coheur, P.-F., Clerbaux, C., Boersma, K. F., van der A, R. and Song, Y.:

933   Substantial Underestimation of Post-Harvest Burning Emissions in the North China

934   Plain Revealed by Multi-Species Space Observations, Sci. Rep., 6, 32307,

935   doi:10.1038/srep32307, 2016.

936   van Donkelaar, A., Martin, R. V., Spurr, R. J. D., Drury, E., Remer, L. A., Levy, R. C.,

937   and Wang, J.: Optimal estimation for global ground-level fine particulate matter

938   concentrations, Journal of Geophysical Research-Atmospheres, 118, 5621-5636,

939   10.1002/jgrd.50479, 2013.

940   Veefkind, J. P., de Haan, J. F., Sneep, M. and Levelt, P. F.: Improvements to the OMI

941   O_2-O_2 operational cloud algorithm and comparisons with ground-based radar–lidar

942   observations, Atmos. Meas. Tech., 9(12), 6035–6049, doi:10.5194/amt-9-6035-2016,

943   2016.

944   Verstraeten, W. W., Neu, J. L., Williams, J. E., Bowman, K. W., Worden, J. R. and

945   Boersma, K. F.: Rapid increases in tropospheric ozone production and export from

946   China, Nat. Geosci., 8, 690 [online] Available from:

947   http://dx.doi.org/10.1038/ngeo2493, 2015.

948   Wang, J., Jacob, D. J. and Martin, S. T.: Sensitivity of sulfate direct climate forcing to

949   the hysteresis of particle phase transitions, J. Geophys. Res. Atmos., 113(D11), n/a-

950   n/a, doi:10.1029/2007JD009368, 2008a.

951   Wang, M., Gu, J., Yang, R., Zeng, L. and Wang, S.: Comparison of cloud type and

952   frequency over China from surface, FY-2E, and CloudSat observations, vol. 9259, pp.

38

953 925913–925914. [online] Available from: http://dx.doi.org/10.1117/12.2069110,

954 2014.

955 Wang, P. and Stammes, P.: Evaluation of SCIAMACHY Oxygen A band cloud

956 heights using Cloudnet measurements, Atmos. Meas. Tech., 7(5), 1331–1350,

957 doi:10.5194/amt-7-1331-2014, 2014.

958 Wang, P., Stammes, P., van der A, R., Pinardi, G. and van Roozendael, M.:

959 FRESCO+: an improved O_2 A-band cloud retrieval algorithm for tropospheric trace

960 gas retrievals, Atmos. Chem. Phys., 8(21), 6565–6576, doi:10.5194/acp-8-6565-2008,

961 2008b.

962 Wang, X., Huang, J., Zhang, R., Chen, B. and Bi, J.: Surface measurements of aerosol

963 properties over northwest China during ARM China 2008 deployment, J. Geophys.

964 Res. Atmos., 115(D7), n/a-n/a, doi:10.1029/2009JD013467, 2010.

965 Wang, Y., Penning de Vries, M., Xie, P. H., Beirle, S., Dörner, S., Remmers, J., Li, A.

966 and Wagner, T.: Cloud and aerosol classification for 2.5 years of MAX-DOAS

967 observations in Wuxi (China) and comparison to independent data sets, Atmos. Meas.

968 Tech., 8(12), 5133–5156, doi:10.5194/amt-8-5133-2015, 2015.

969 Wang, Y., Lampel, J., Xie, P., Beirle, S., Li, A., Wu, D. and Wagner, T.: Ground-

970 based MAX-DOAS observations of tropospheric aerosols, NO_2, SO_2 and HCHO in

971 Wuxi, China, from 2011 to 2014, Atmos. Chem. Phys., 17(3), 2189–2215,

972 doi:10.5194/acp-17-2189-2017, 2017a.

973 Wang, Y., Beirle, S., Lampel, J., Koukouli, M., De Smedt, I., Theys, N., Li, A., Wu,

974 D., Xie, P., Liu, C., Van Roozendael, M., Stavrakou, T., Müller, J.-F. and Wagner, T.:

975 Validation of OMI, GOME-2A and GOME-2B tropospheric NO_2, SO_2 and HCHO

976 products using MAX-DOAS observations from 2011 to 2014 in Wuxi, China:

977   investigation of the effects of priori profiles and aerosols on the satellite products,

978   Atmos. Chem. Phys., 17(8), 5007–5033, doi:10.5194/acp-17-5007-2017, 2017b.

979   Winker, D. M., Pelon, J., Coakley, J. A., Ackerman, S. A., Charlson, R. J., Colarco, P.

980   R., Flamant, P., Fu, Q., Hoff, R. M., Kittaka, C., Kubar, T. L., Le Treut, H.,

981   Mccormick, M. P., Mégie, G., Poole, L., Powell, K., Trepte, C., Vaughan, M. A. and

982   Wielicki, B. A.: The CALIPSO Mission, Bull. Am. Meteorol. Soc., 91(9), 1211–

983   1230, doi:10.1175/2010BAMS3009.1, 2010.

984   Winker, D. M., Tackett, J. L., Getzewich, B. J., Liu, Z., Vaughan, M. A. and Rogers,

985   R. R.: The global 3-D distribution of tropospheric aerosols as characterized by

986   CALIOP, Atmos. Chem. Phys., 13(6), 3345–3361, doi:10.5194/acp-13-3345-2013,

987   2013.

988   Zara, M., Boersma, K. F., De Smedt, I., Richter, A., Peters, E., Van Geffen, J. H. G.

989   M., Beirle, S., Wagner, T., Van Roozendael, M., Marchenko, S., Lamsal, L. N. and

990   Eskes, H. J.: Improved slant column density retrieval of nitrogen dioxide and

991   formaldehyde for OMI and GOME-2A from QA4ECV: intercomparison, uncertainty

992   characterization, and trends, Atmos. Meas. Tech. Discuss., 1–47, doi:10.5194/amt-

993   2017-453, 2018.

994   Zhang, Q., Streets, D. G., Carmichael, G. R., He, K. B., Huo, H., Kannari, A.,

995   Klimont, Z., Park, I. S., Reddy, S., Fu, J. S., Chen, D., Duan, L., Lei, Y., Wang, L. T.

996   and Yao, Z. L.: Asian emissions in 2006 for the NASA INTEX-B mission, Atmos.

997   Chem. Phys., 9(14), 5131–5153, doi:10.5194/acp-9-5131-2009, 2009.

998   Zhao, C. and Wang, Y.: Assimilated inversion of NO_X emissions over east Asia using

999   OMI NO_2 column measurements, Geophys. Res. Lett., 36(6), L06805,

1000   doi:10.1029/2008GL037123, 2009.

1001   Zhao, H. Y., Zhang, Q., Guan, D. B., Davis, S. J., Liu, Z., Huo, H., Lin, J. T., Liu, W.

1002   D. and He, K. B.: Assessment of China's virtual air pollution transport embodied in

1003   trade by using a consumption-based emission inventory, Atmos. Chem. Phys., 15(10),

1004   5443–5456, doi:10.5194/acp-15-5443-2015, 2015.

1005   Zhou, Y., Brunner, D., Spurr, R. J. D., Boersma, K. F., Sneep, M., Popp, C. and

1006   Buchmann, B.: Accounting for surface reflectance anisotropy in satellite retrievals of

1007   tropospheric NO_2, Atmos. Meas. Tech., 3(5), 1185–1203, doi:10.5194/amt-3-1185-

1008   2010, 2010.

1009   Zhu, W., Xu, C., Qian, X. and Wei, H.: Statistical analysis of the spatial-temporal

1010   distribution of aerosol extinction retrieved by micro-pulse lidar in Kashgar, China,

1011   Opt. Express, 21(3), 2531–2537, doi:10.1364/OE.21.002531, 2013.

1012

1013

Table A1. Number of CALIOP observations in a grid cell (0.667°× 0.5°).

	Before filtering				After filtering			
	Mean	Median	Minima	Maximum	Mean	Median	Minima	Maximum
For a month	165	169	0	291	47	39	0	223
For the same month in nine years	1483	1513	192	1921	420	395	0	1548
For all months in nine years	17794	18528	5608	20781	5033	5381	146	12650

1014

Table 1. MAX-DOAS measurement sites and corresponding meteorological stations.

MAX-DOAS site name	Site information	Measurement times	Corresponding meteorological station name	Meteorological station information
Xianghe	116.96^{o}E, 39.75^{o}N, 36 m, suburban	2012/01/01 -2012/12/31	CAPITAL INTERNATIONA	116.89^{o}E, 40.01^{o}N, 35.4 m
IAP	116.38^{o}E, 39.98^{o}N, 92 m, urban	2008/06/22 -2009/04/16	CAPITAL INTERNATIONA	116.89^{o}E, 40.01^{o}N, 35.4 m
Wuxi	120.31^{o}E, 31.57^{o}N, 20 m, urban	2012/01/01 -2012/12/31	HONGQIAO INTL	121.34^{o}E, 31.20^{o}N, 3 m

1015

43

Table 1. MAX-DOAS measurement sites and corresponding meteorological stations.

MAX-DOAS site name	Site information	Measurement times	Corresponding meteorological station	Meteorological station
	39.75^{o}N, 36 m,		INTERNATIONA	40.01^{o}N, 35.4 m

Table 2. Evaluation of OMI NO_2 products with respect to MAX-DOAS on 27 haze days [1].

	POMINO v1.1	POMINO	DOMINO v2	QA4ECV
Slope	1.07	0.80	1.11	0.58
Intercept	-3.58	1.76	-11.79	3.20
(10^{15} molec./cm^2)				
R^2	0.76	0.68	0.38	0.34
NMB (%)	4.4	-9.4	-5.0	-26.11

1016 1. The haze days are determined when the ground meteorological station data and
1017   MODIS/Aqua corrected reflectance (true color) data both indicate a haze day.
1018   Average across the days, AOD = 1.13 (median = 1.10), SSA = 0.90 (0.91), MAX-
1019   DOAS NO_2 = 51.92 x 10^{15} molec. cm^{-2}, and CF = 0.06 (0.03).

Table 3. Evaluation of OMI NO_2 products with respect to MAX-DOAS on 36 cloud-free days [1].

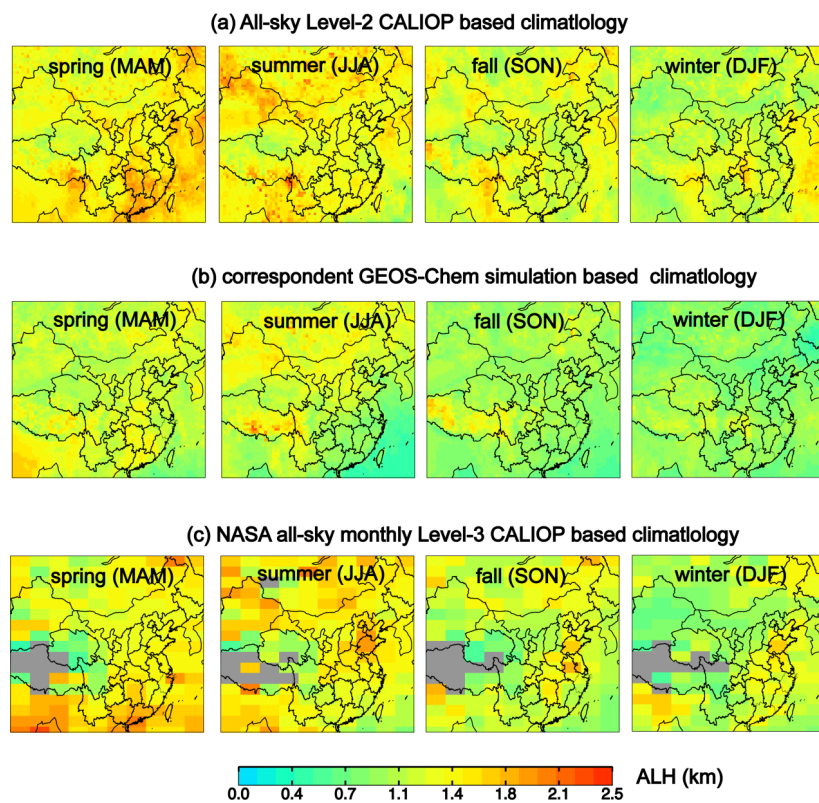|	POMINO v1.1	POMINO	DOMINO v2	QA4ECV
Slope	1.30	1.13	0.92	0.79
Intercept	-0.61	0.31	2.32	1.05
R^2	0.55	0.56	0.53	0.63
NMB (%)	29.4	20.8	21.9	-5.83

1020   1. CF=0 in POMINO product. Average across the days, AOD = 0.60 (median = 0.47),

1021   SSA = 0.90 (0.91), and MAX-DOAS NO_2 = 26.82 x 10^{15} molec. cm^{-2}.

(a) The total number before filtering

(b) The total number after filtering
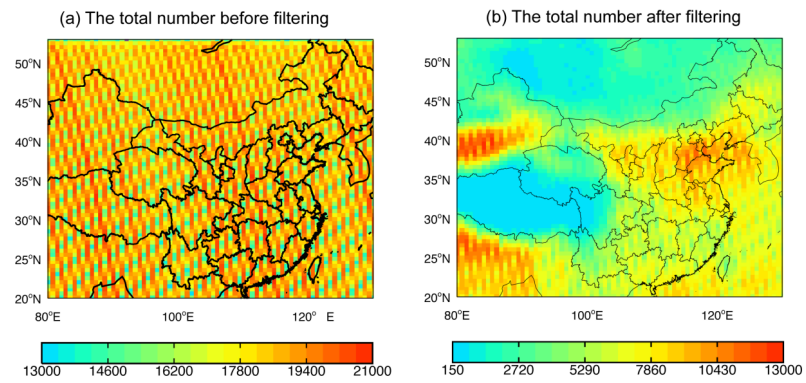
1022   Figure A1. The total number of CALIOP Level-2 aerosol extinction profiles at 532 nm

1023   used to derive our climatological (2007–2015) dataset on a 0.667° long. x 0.5° lat. grid
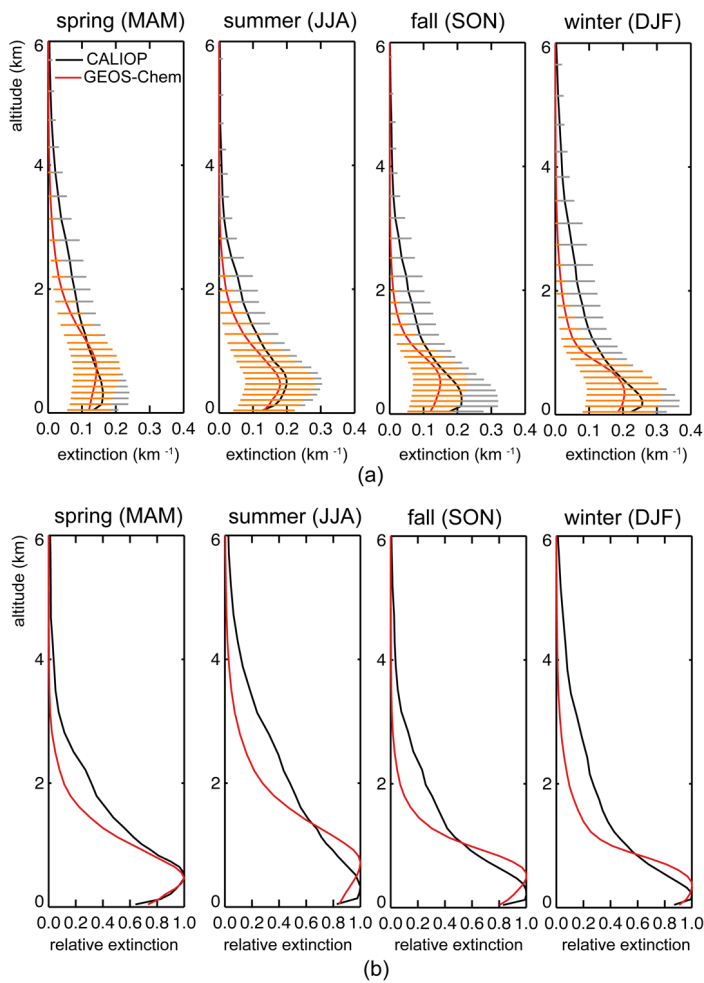
1024   (a) before and (b) after filtering.
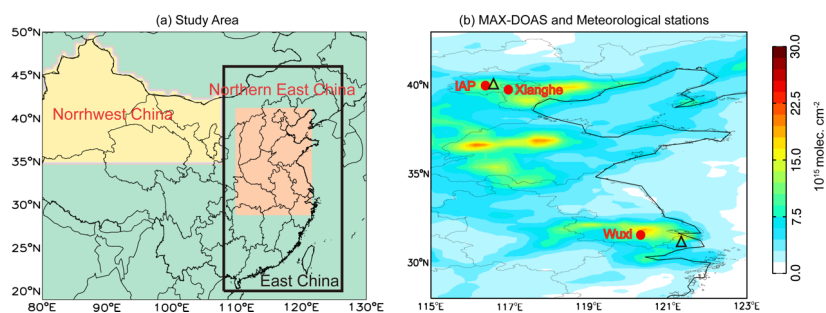
1025 Figure 1. (a) Three study areas: Northern East China, Northwest China, and East China.

1026 (b) MAX-DOAS measurement sites (red dots) and corresponding meteorological

1027 stations (black triangle) overlaid on POMINO v1.1 NO$_2$ VCDs in August 2012.

47

(a) All-sky Level-2 CALIOP based climatlology

spring (MAM) summer (JJA) fall (SON) winter (DJF)

(b) correspondent GEOS-Chem simulation based climatlology

spring (MAM) summer (JJA) fall (SON) winter (DJF)

(c) NASA all-sky monthly Level-3 CALIOP based climatlology

spring (MAM) summer (JJA) fall (SON) winter (DJF)

ALH (km)
0.0 0.4 0.7 1.1 1.4 1.8 2.1 2.5

1028   Figure 2. Seasonal spatial patterns of ALH climatology at 532 nm on a 0.667° long. x

1029   0.50 ° lat. grid based on (a) our complied all-sky Level-2 CALIOP data, (b)

1030   corresponding GEOS-Chem simulations, and (c) NASA all-sky monthly Level-3

1031   CALIOP dataset.

48
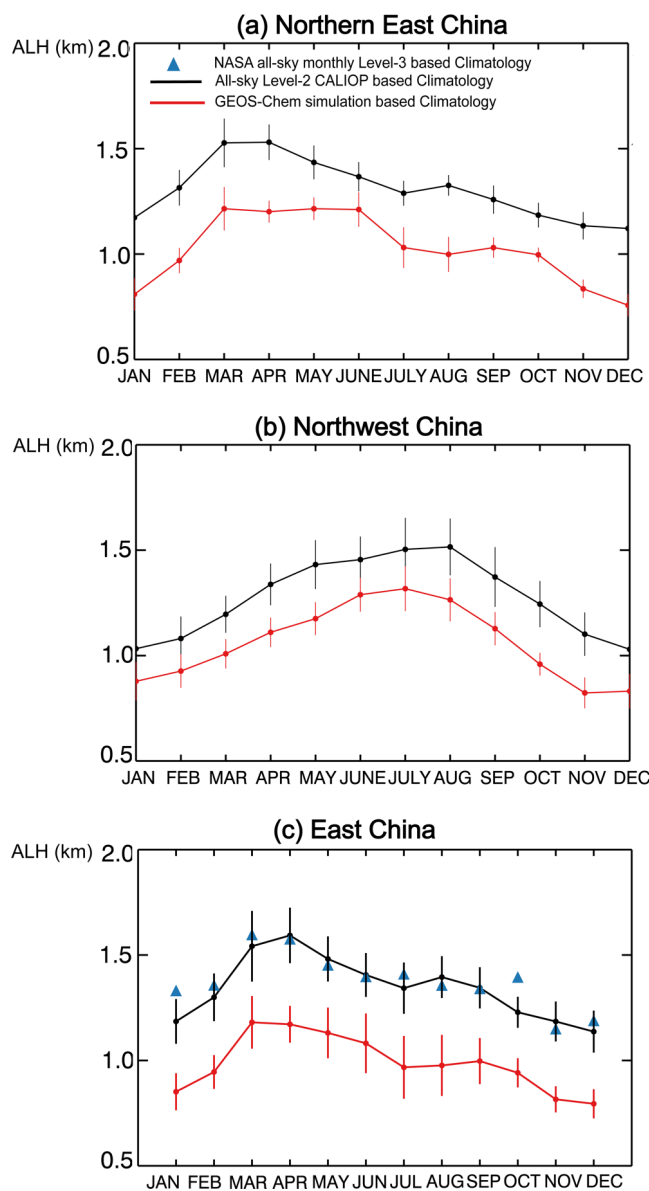
Figure 3. Regional mean ALH monthly climatology over (a) Northern East China, (b) Northwest China, and (c) East China. The error bars stand for 1 standard deviation for spatial variability.

spring (MAM) summer (JJA) fall (SON) winter (DJF)

(a)

spring (MAM) summer (JJA) fall (SON) winter (DJF)

(b)

Figure 4. Seasonal climatological aerosol extinction profiles (first row) and corresponding relative extinction profiles (normalized to maximum extinction values, second raw) in spring (MAM), summer (JJA), fall (SON) and winter (DJF) over Northern East China. Model results (in red) are prior to MODIS/Aqua based AOD adjustment. Error bars in (a) represent 1 standard deviation across all grid cells in each season.

(a)

(b)
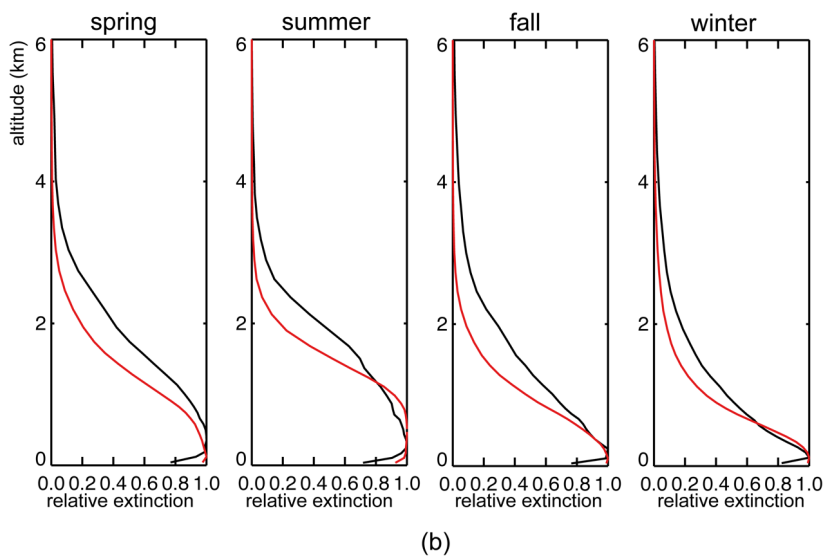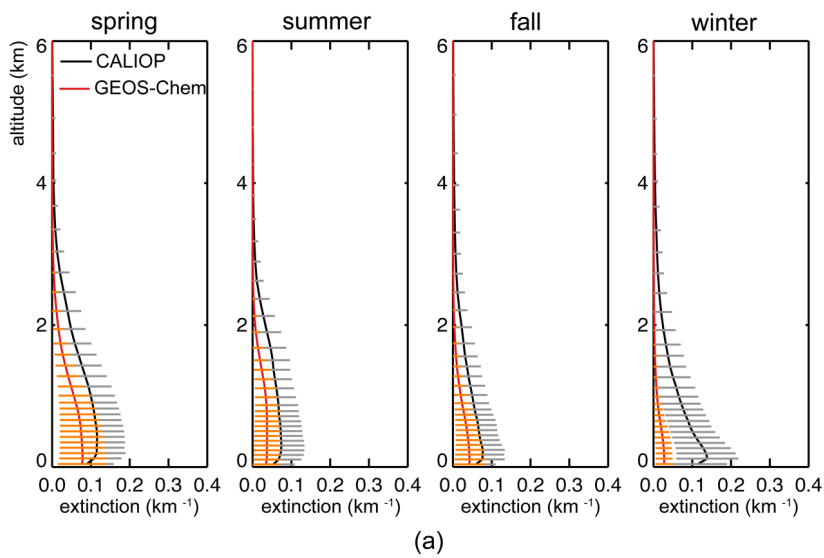
1042   Figure 5. Similar to Fig. 5 but for Northwest China.

51
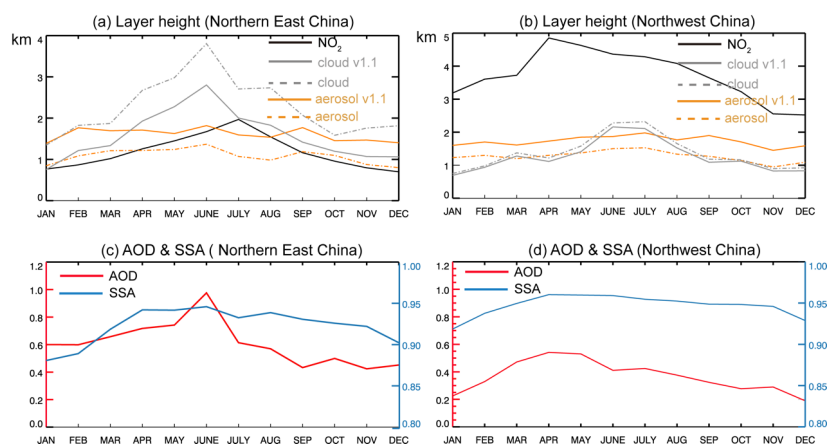
Figure 6. Monthly variations of ALH, CTH and NLH over (a) Northern East China and (b) Northwest China in 2012. Data are averaged across all pixels in each month and region. The grey and orange solid lines denote POMINO v1.1 results, while the corresponding dashed lines denote POMINO. (c–d) Corresponding monthly AOD and SSA.
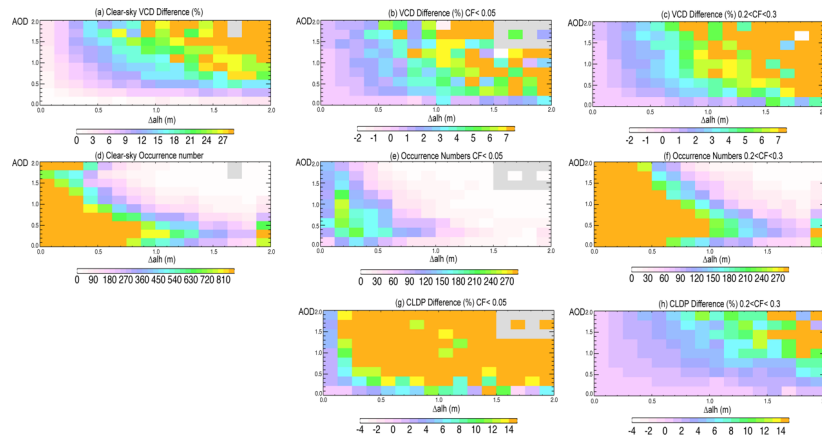
Figure 7. Percentage changes in VCD from POMINO to POMINO v1.1 ([POMINO v1.1 – POMINO] / POMINO) for each bin of ΔALH (bin size = 0.2 km) and AOD (bin size = 0.1) across pixels in 2012 over Northern East China, for (a) cloud-free sky (CF = 0 in POMINO), (b) little-cloudy sky, and (c) modestly cloudy sky. (d-f) The number of occurrences corresponding to (a-c). (g, h) Similar to (b, c) but for the percentage changes in cloud top pressure (CP).

53
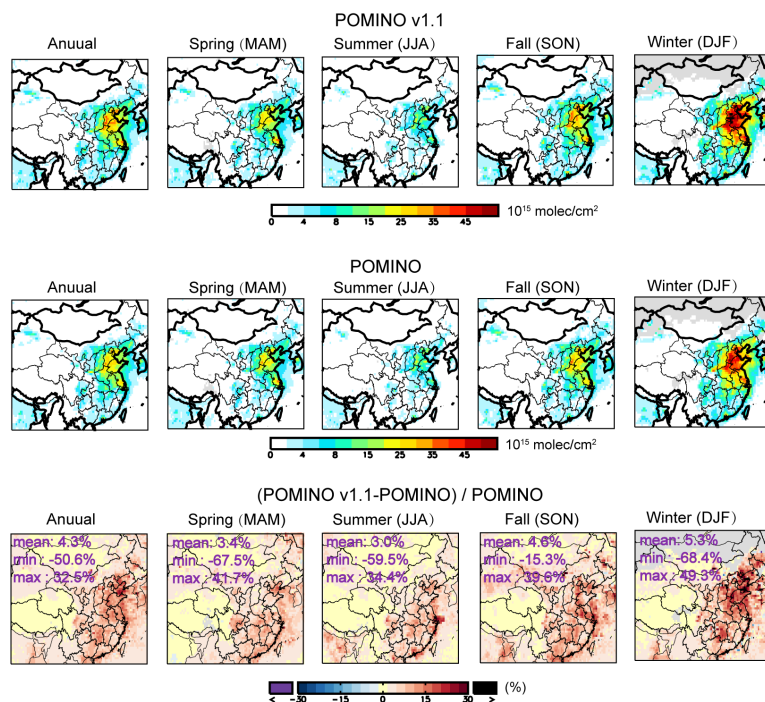
Figure 8. Seasonal spatial distribution of tropospheric NO$_2$ VCD in 2012 for (a)
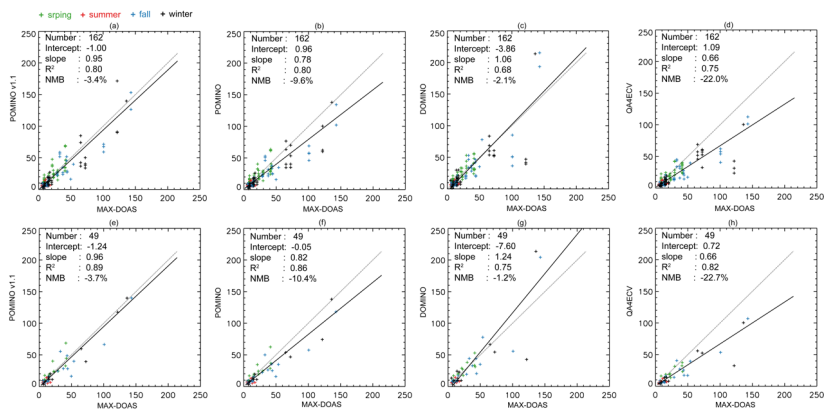POMINO v1.1, (b) POMINO, and (c) their relative difference.

Figure 9. (a–d) Scatterplot for NO$_2$ VCDs (10^{15} molec. cm^{-2}) between MAX-DOAS and each of the three OMI products. Each "+" corresponds to an OMI pixel, as several pixels may be available in a day. (e–h) Similar to (a–d) but after averaging over all OMI pixels in the same day, such that each "+" represents a day. Also shown are the statistic results from the RMA regression. The black solid line indicates the regression curve and the grey dotted line depict the 1:1 relationship.